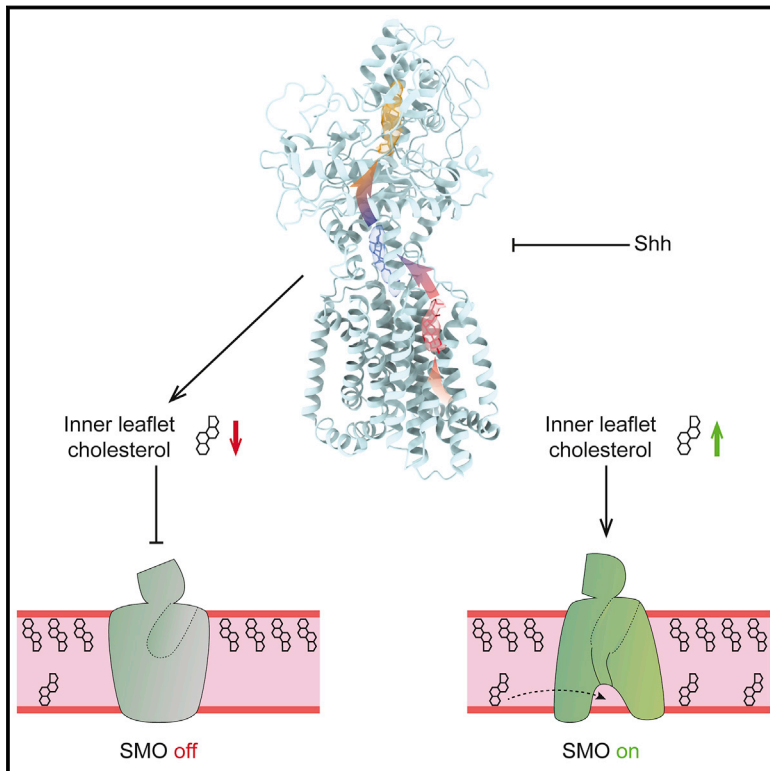Article

# Structural Basis for Cholesterol Transport-like Activity of the Hedgehog Receptor Patched

## Graphical Abstract

## Authors

Yunxiao Zhang, David P. Bulkley,
Yao Xin, ..., Wonhwa Cho, Yifan Cheng,
Philip A. Beachy

## Correspondence

wcho@uic.edu (W.C.),
yifan.cheng@ucsf.edu (Y.C.),
pbeachy@stanford.edu (P.A.B.)

## In Brief

Structural and biochemical evidence suggests that the Hedgehog receptor Patched may mediate removal of cholesterol from the inner leaflet of the plasma membrane via a hydrophobic conduit.

## Highlights

- Patched structure reveals a hydrophobic conduit with sterol-like contents

- Patched mediates Hedgehog-reversible reduction of inner leaflet cholesterol activity

- Hydrophobic conduit is essential for cholesterol effect and Smoothened suppression

- Inner leaflet cholesterol likely mediates Hedgehog-Patched regulation of Smoothened

CellPress

# Structural Basis
# for Cholesterol Transport-like Activity
# of the Hedgehog Receptor Patched

Yunxiao Zhang,[1,2,9] David P. Bulkley,[3,9] Yao Xin,[4,9] Kelsey J. Roberts,[1,5] Daniel E. Asarnow,[3] Ashutosh Sharma,[4] Benjamin R. Myers,[1,8] Wonhwa Cho,[4,*] Yifan Cheng,[3,7,*] and Philip A. Beachy[1,2,5,6,10,*]

[1]Institute for Stem Cell Biology and Regenerative Medicine, Stanford University School of Medicine, Stanford, CA 94305, USA
[2]Howard Hughes Medical Institute, Stanford University School of Medicine, Stanford, CA 94158, USA
[3]Department of Biochemistry and Biophysics, University of California, San Francisco, San Francisco, CA 94158, USA
[4]Department of Chemistry, University of Illinois at Chicago, Chicago, IL 60607, USA
[5]Department of Developmental Biology, Stanford University School of Medicine, Stanford, CA 94305, USA
[6]Departments of Biochemistry and Urology, Stanford University School of Medicine, Stanford, CA 94305, USA
[7]Howard Hughes Medical Institute, University of California, San Francisco, San Francisco, CA 94158, USA
[8]Present address: Department of Oncological Sciences, Huntsman Cancer Institute, University of Utah School of Medicine, Salt Lake City, UT 84112, USA
[9]These authors contributed equally
[10]Lead Contact
*Correspondence: wcho@uic.edu (W.C.), yifan.cheng@ucsf.edu (Y.C.), pbeachy@stanford.edu (P.A.B.)
 https://doi.org/10.1016/j.cell.2018.10.026

## SUMMARY

Hedgehog protein signals mediate tissue patterning and maintenance by binding to and inactivating their common receptor Patched, a 12-transmembrane protein that otherwise would suppress the activity of the 7-transmembrane protein Smoothened. Loss of Patched function, the most common cause of basal cell carcinoma, permits unregulated activation of Smoothened and of the Hedgehog pathway. A cryo-EM structure of the Patched protein reveals striking transmembrane domain similarities to prokaryotic RND transporters. A central hydrophobic conduit with cholesterol-like contents courses through the extracellular domain and resembles that used by other RND proteins to transport substrates, suggesting Patched activity in cholesterol transport. Cholesterol activity in the inner leaflet of the plasma membrane is reduced by PTCH1 expression but rapidly restored by Hedgehog stimulation, suggesting that PTCH1 regulates Smoothened by controlling cholesterol availability.

## INTRODUCTION

The Hedgehog (Hh) family of secreted protein signals patterns many tissues and structures during embryogenesis (Chiang et al., 1996; Dessaud et al., 2008; Ingham, 1993) and, post-embryonically, governs tissue homeostasis and regeneration by regulating stem cell activity (Goodrich et al., 1997; Shin et al., 2011; Teglund and Toftgård, 2010). Impaired Hedgehog signaling is associated with birth defects, including holoprosencephaly (HPE) (Chiang et al., 1996; Roessler et al., 1996),

whereas aberrant pathway activation leads to formation of ecto-dermally derived cancers such as basal cell carcinoma (BCC) and medulloblastoma (Teglund and Toftgård, 2010). Recent work also reveals that pathway activity in stromal cells actually restrains cancer growth and progression in certain cancers of endodermal origin (Gerling et al., 2016; Lee et al., 2014, 2016; Rhim et al., 2014; Shin et al., 2014).

The mammalian Hedgehog family comprises Sonic hedgehog (SHH), Desert hedgehog (DHH), and Indian hedgehog (IHH), which diverge in their expression patterns, but all utilize a common transduction machinery. The major receptor for mammalian Hedgehog signals is Patched1 (PTCH1) (Chen and Struhl, 1996; Fuse et al., 1999; Ingham et al., 1991; Stone et al., 1996), a 12-pass transmembrane protein. PTCH1 suppresses activity of the 7-pass transmembrane protein Smoothened (SMO), maintaining Hedgehog pathway quiescence. When PTCH1 is bound by Hedgehog, PTCH1 suppression of SMO is lifted, permitting SMO-mediated pathway activation (Goodrich et al., 1997; Ingham and McMahon, 2001; Ingham et al., 1991; Figure S1A). PTCH1 binding also serves to sequester the Hedgehog protein, shaping graded tissue responses to Hedgehog signals. Both SMO regulation and Hedgehog sequestration are conserved in metazoans ranging from insects to mammals (Chen and Struhl, 1996; Ingham and McMahon, 2001) and are needed to prevent inappropriate pathway activity. Loss-of-function *PTCH1* mutations account for about 85% of BCC (Johnson et al., 1996), a cancer with over 1 million patients treated annually in the United States alone (Rogers et al., 2015), making *PTCH1* perhaps the most commonly mutated tumor suppressor.

Little is known regarding the biochemical function of PTCH1. Several observations, including homology of PTCH1 to the resistance-nodulation-division (RND) family of bacterial transporters, led to a model suggesting that PTCH1 may act as a transporter that controls access of certain modulatory lipids to SMO, with the binding of Hedgehog acting to inhibit this transport activity

(Taipale et al., 2002). A large body of work encompassing genetic, cell biological, biochemical, and structural approaches has shown that cholesterol is required for SMO activation (Byrne et al., 2016; Cooper et al., 2003; Huang et al., 2016, 2018; Luchetti et al., 2016; Myers et al., 2013, 2017; Xiao et al., 2017). Whether PTCH1 regulates SMO by acting on cellular cholesterol has not been addressed.

We have succeeded in preparing a biochemically well-behaved PTCH1 protein that is active in high-affinity Hedgehog protein binding and is suitable for structural investigation. In this study, we report an electron cryo-microscopy (cryo-EM) structure of mouse PTCH1 with an overall resolution of 3.6 Å. Our analysis of structural elements and topology of the PTCH1 extracellular domains reveals similarities to NPC1 and RND proteins. A particularly striking feature of the PTCH1 structure is the presence of a hydrophobic conduit that courses through the extracellular domain, with cholesterol-like densities within and at either end of the conduit. PTCH1 expression reduces inner plasma membrane cholesterol activity in a manner dependent on the integrity of the hydrophobic conduit, and ShhN rapidly reverses this change. These findings together suggest that PTCH1 may transport membrane cholesterol and, thus, supply a missing link in our understanding of the mechanism by which PTCH1 regulates SMO.

## RESULTS

### Preparation of a Stable PTCH1 Variant

The full-length mouse PTCH1 protein is poorly expressed and biochemically unstable (Cleveland et al., 2014). We sought to identify a more stable protein variant by using FSEC (fluorescence detection size exclusion chromatography (Kawate and Gouaux, 2006)) to screen constructs from which potential destabilizing sequences were deleted. Two HECT E3 ubiquitin ligase interaction sites are present in mouse PTCH1, one within the cytoplasmic loop between transmembrane helices TM6 and TM7 and the other in the C-terminal cytoplasmic domain (Kim et al., 2015). A previously reported C-terminal truncation, Ptc-CTD (here referred to as Ptch1-A), removes the latter of these HECT E3 sites and boosts PTCH1 expression (Fuse et al., 1999; Kim et al., 2015; Lu et al., 2006). The final construct we selected, hereafter referred to as Ptch1-B, bears an additional deletion that removes the first HECT E3 site within the large cytoplasmic loop and results in an even higher level of expression and biochemical behavior as a monodisperse peak in FSEC (Figure S1B; deletion shown in the sequence alignment in Figure S1C).

We measured the *in vivo* activity of the Ptch1-B variant with a conventional Gli-dependent luciferase reporter assay in *Ptch1*$^{-/-}$ mouse embryonic fibroblasts (MEFs). Because of the absence of *Ptch1* function, these cells show constitutively high activity and no additional activation by Hedgehog stimulation (Taipale et al., 2002). Introduction of the Ptch1-B expression construct suppressed this high basal activity and rendered cells responsive to the ShhN protein ligand, demonstrating that the stabilized Ptch1-B variant maintains *in vivo* activity similar to that of full-length wild-type PTCH1 (Figure 1A). We then purified Ptch1-B from HEK293 cells using the BacMam expression sys-

tem (STAR Methods). Size exclusion chromatography (SEC) of the purified protein revealed an essentially monodisperse near-Gaussian peak, indicating biochemical homogeneity (Figure S1D). Using microscale thermophoresis, we found that the GFP-tagged ShhN (SHH signaling domain) binds Ptch1-B at 27 ± 14 nM affinity (Figure 1B), close to previous measurements of ShhN binding to full-length PTCH1 on the cell surface (Fuse et al., 1999). This result suggests that the purified protein maintains its physiological fold and also indicates that, unlike *Drosophila* Ptc, which requires an Ihog family co-receptor to engage Hedgehog (Zheng et al., 2010), mouse Ptch1 alone is sufficient for high-affinity Hedgehog binding, confirming that the mode of Hh-receptor interaction has diverged between insects and mammals (McLellan et al., 2008).

### Overview of PTCH1 Structure

We determined a single-particle cryo-EM structure of Ptch1-B (Figure S2). This structure has an overall resolution of 3.7 Å (Figures 1C, 1D, and S3F) and reveals a homodimer with the transmembrane domain of one monomer resolved significantly better than that of the other. The extracellular domains in this map, however, appear to be symmetrical. Imposition of C2 symmetry improved the overall resolution to 3.5 Å (Figure S3H) but worsened features in the TM domain of the better-resolved subunit (Figures S3E and S3G). Separating each dimer into two individual particles and refining them in concert produced the best map of the monomer (3.6 Å; map shown in Figure 1E; resolution in Figure S3J); this improvement resulted from reducing the uncertainty of monomer positions within the dimer (see below).

Our maps permitted reliable de novo construction of an atomic model of PTCH1 (Figures 1F, S4A, and S4B; see also Table 1). In the final model, secondary structures match primary sequence predictions. Furthermore, the positions of 6 highly conserved cysteines in the extracellular loop between TM1 and TM2 (hereafter ECD1) permit formation of 3 disulfide bonds (residues are shown in the sequence alignment in Figure S1C; density is shown in Figure S4A; schematically drawn in Figures S4C and S4D), suggesting that the model correctly threads the primary sequence through the map, with side chains in appropriate register.

Our PTCH1 model exhibits a typical RND transporter-like domain organization (Figure 1G). Twelve transmembrane helices cluster together to form the transmembrane domain, with pseudo 2-fold symmetry between TM1–TM6 and TM7–TM12 (Figure S4E). Two large extracellular domains are located between TM1 and TM2 (ECD1) and between TM7 and TM8 (hereafter ECD2). Most of the intracellular sequence is unresolved, except for two transverse helices preceding TM1 and TM7 at the cytoplasmic face of the protein (Figure 1F). Although the Ptch1-B protein sample was prepared by ShhN-mediated elution from an ShhN affinity matrix, no density corresponding to the ShhN protein is present in the map, suggesting that the complex of ShhN with the Ptch1-B dimer is de-stabilized during cryo-EM grid preparation.

### PTCH1 Dimer Interface

A remarkable feature of our structure is its dimeric architecture, in which monomer association is mediated exclusively by the
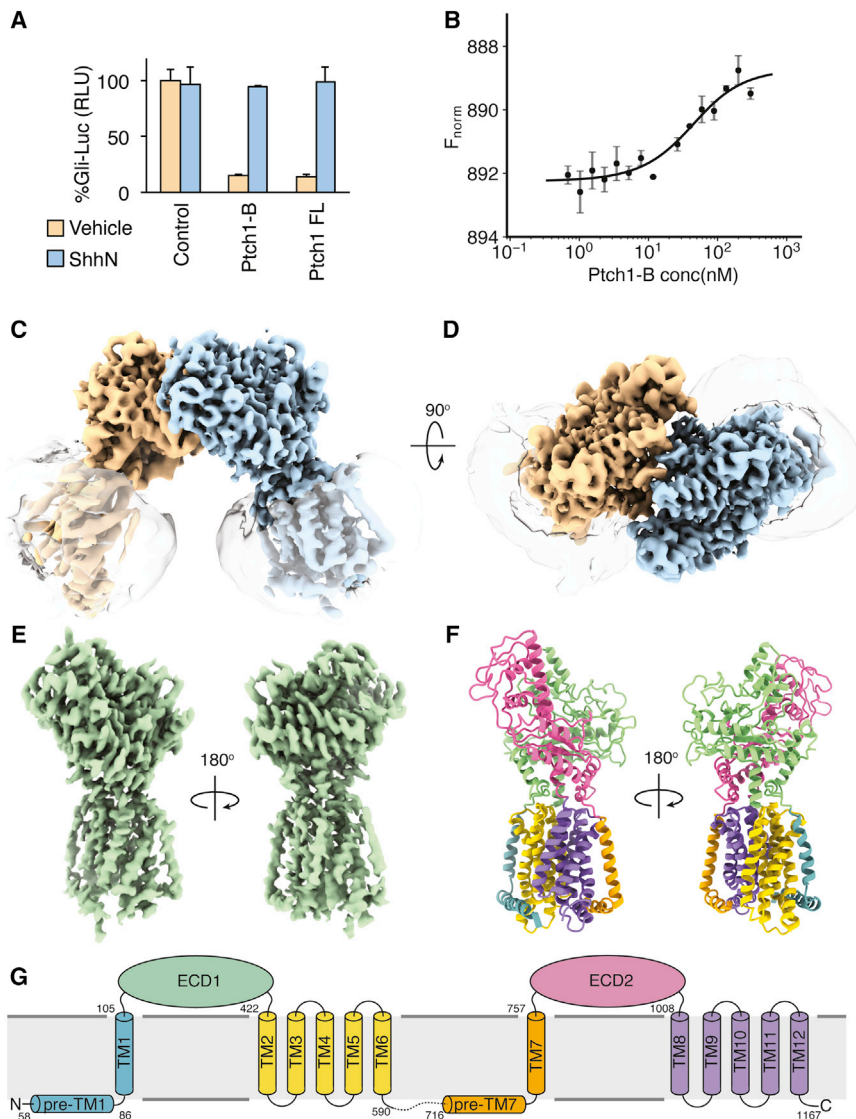
**Figure 1. Activity, Purification, and Structure of the PTCH1 Protein**

(A) The activity of PTCH1 variants was tested in a Gli-dependent luciferase assay in $Ptch1^{-/-}$ cell lines. Full-length Ptch1 (FL) or the stabilized Ptch1-B variant suppressed high basal activity of $Ptch1^{-/-}$ cells and responded to SHH ligand, whereas control cells showed maximal pathway activation. Data for each condition were averaged from triplicates, with error bars indicating SEM.

(B) The affinity of the Ptch1-B variant for GFP-tagged ShhN protein was measured by microscale thermopheresis (MST). The affinity derived from the standard $K_d$ equation is $27 \pm 14$ nM. Data for each concentration were averaged from technical duplicates, with error bars indicating SEM.

(C and D) The cryo-EM map of the Ptch1-B sample is shown in side view (C), from within the plane of the membrane, and in top view (D, extracellular perspective), with subunits colored differently. Note the detergent micelles, shown as transparent shells shrouding the transmembrane domains.

(E) The refined 3.6-Å resolution PTCH1 monomer map.

(F) The PTCH1 atomic model. Domains are colored as follows: pre-TM1 helix and TM1, malachite; extracellular domain 1 (ECD1), lime; TM2–TM7, yellow; pre-TM7 and TM7, orange; extracellular domain 2 (ECD2), pink; TM8–TM12, lavender.

(G) Schematic view of PTCH1 domains, colored as in (F).

extracellular domains, with the two transmembrane domains projecting away from this vertex at an angle of roughly 50°. This architecture is unusual among membrane proteins of known structure. The angle between the transmembrane domains implies a positive curvature with a radius of ~9 nm in the associated membrane. The dimeric oligomerization state is further supported by SEC-multi-angle light scattering (MALS) analysis of purified Ptch1-B in amphipol A8-35, which yields a molecular mass of 286 kDa, consistent with a PTCH1 dimer (Figure S5A).

We constructed a model of the dimer by placing the monomeric atomic structure into the C2 symmetrized map. In this model, the dimer interface consists of mostly hydrophobic interactions, the tightest being those mediated by residues Y233, I234, and I235 near the center of C2 symmetry (Figures 2A and 2B). Other less central residues, however, also contribute (Figures 2C and 2D). The limited number of residues at the dimer interface may impart considerable flexibility to the dimer and, in part, account for the

lower resolution of one subunit in the non-symmetrized map. Indeed, in our multibody analysis treating each subunit independently for alignment (Figures S2 and S5B), we observed significant flexibility between the two subunits within a dimer (Figure S5C; principal components analyzed in Figures S5D and S5E; see also Video S1). Nonetheless, no major differences in conformation are apparent within monomers at the resolution of our maps (Figure S5F).

We tested the *in vivo* occurrence of the PTCH1 dimer by introducing Cys substitutions designed to mediate disulfide bond formation between monomers. Upon cysteine substitution at the residues close to the core of the dimer interface (namely, Y233, I234, and I235; Figure 2B), we noted, by western blotting, the appearance of a band corresponding to a cross-linked dimer, with collapse of this band into a monomer band in the presence of a reducing agent (Figure 2E). This type of reversible cross-linking confirms the proximity of the Cys-substituted residues at the dimer interface. The prevalence of the dimer band in the absence of any oxidizing agents suggests that a significant fraction of PTCH1 exists as a dimer under these overexpression conditions.

The Cys-substituted proteins displayed normal function in SMO suppression and ShhN signal response upon introduction into $Ptch1^{-/-}$ MEFs (Figure 2F), raising a question regarding

**Table 1. Summary of Cryo-EM Data Collection and Model Refinement**

| Data Collection/Processing | |
| --- | --- |
| Voltage (kV) | 300 |
| Magnification | 22,500 |
| Defocus range (μm) | −1.0 to −3.0 |
| Pixel size (Å) | 1.31 |
| Total electron dose (e$^-$/Å$^2$) | 38 |
| Exposure time (s) | 8 |
| Number of images | 5,236 |
| Number of frames/image | 40 |
| Initial particle number | 1,302,704 (autopick) |
| | 378,828 (2D select) |
| Final particle number | 245,725 |
| Resolution (unmasked, Å) | 4.17 |
| Resolution (masked, Å) | 3.60 |
| Refinement | |
| Number of atoms | 6,910 |
| RMSDs | |
| Bond lengths (Å) | 0.007 |
| Bond angles (º) | 1.399 |
| Ramachandran | |
| Favored (%) | 92.65 |
| Allowed (%) | 7.35 |
| Outlier (%) | 0.00 |
| Molprobity score | 2.90 |
| EMRinger score | 2.68 |

the physiologic function of PTCH1 dimerization. Attempts to break the PTCH1 dimer by altering residues at the dimer interface also did not reveal a change in PTCH1 activity (Figure 2G). We note, in three other recently published structures (Gong et al., 2018; Qi et al., 2018a, 2018b) that the ShhN::PTCH1 interfaces are incompatible with the dimer architecture we observe. The observation that Cys-substituted proteins respond to ShhN suggests that PTCH1 dimerization may be minimal at the low expression levels permitting ligand regulated transcriptional response; the physiologic relevance of this observed dimerization awaits future investigation.

## Transporter-like Features of PTCH1

Comparison of the PTCH1 structure with related structures from other RND homologs reveals essentially the same fold of their transmembrane domains. The PTCH1 transmembrane domain can be superimposed onto those of AcrB, SecDF, HpnN, and NPC1 with root-mean-square deviation (RMSD) values of 6.08 Å, 5.10 Å, 6.85 Å, and 1.95 Å, respectively (Figure 3A; Figure S6A).

In most well-characterized bacterial RND transporters, the transmembrane domain drives the conformational cycling required for transport by conducting ion flow through a pathway lined by a triad of charged residues in TM4 and TM10. This charged triad is conserved in PTCH1 (Figure 3C), and we tested

its importance by introducing the charge-neutralizing alterations D499N, D500N, and E1081Q (referred to as NNQ). This NNQ variant is no longer able to suppress SMO upon introduction into the *Ptch1*$^{-/-}$ cell line (Figure 3E; also reported in Myers et al., 2017) but retains the ability to bind ShhN (Figure 3F), consistent with the possibility that the PTCH1 transmembrane domain may utilize ion flow to drive a conformational cycle required for its function.

The extracellular domain of PTCH1, in contrast, is more distinctive, containing not only conserved but also highly divergent features (Figure S6B). The conserved feature common to the extracellular, periplasmic, or lumenal domains of all of these proteins is an "open face" α+β sandwich fold consisting of two α helices and three strands (Figure 3G). A variation of this theme is seen in AcrB, in which each periplasmic domain comprises two α+β sandwich domains (Figure S6B), the first one uninterrupted and the second one interrupted by the "TolC docking domain" (see below). In SecDF, the insertion is between helix 2 and strand 3, rather than between helix 1 and strand 2 (Figure S6B).

It is noteworthy that amino acid sequences inserted into the conserved α+β sandwich fold are associated with the unique activity of each protein. In AcrB, this insertion (the TolC docking domain) docks to the TolC protein conduit for substrate extrusion through the outer membrane (Koronakis et al., 2000; Tamura et al., 2005); in NPC1, the insertion contains the site for binding of NPC2, a docking partner required for cholesterol transfer (Li et al., 2016), and for binding of glycoproteins of filoviruses, including Ebola, which exploit NPC1 for entry into host cells (Wang et al., 2016). In SecDF, the insertion is the head domain, proposed to function in peptide translocation (Tsukazaki and Nureki, 2011). The insertion in ECD1 and ECD2 of PTCH1 constitutes the Hedgehog binding site (Gong et al., 2018; Qi et al., 2018a). Given the conservation of the transmembrane domain and the presence of the α+β sandwich fold in both extracellular loops, it is likely that the ancestral progenitor of these proteins comprised a six-transmembrane protein with a single large loop protruding between TM1 and TM2 and containing one or two sandwich folds; these sandwich folds then evolved further to incorporate various insertions dedicated to particular functions, either before or after duplication of the entire six-transmembrane domain to generate the modern 12-transmembrane topology (Figure 4). NPC1 then acquired an additional transmembrane and luminal domain extension of its N terminus. Among bacterial RND homologs of known structure, the overall domain organization of PTCH1 most resembles that of the *Burkholderia multivorans* transporter HpnN, required for hopanoid export to the outer membrane (Kumar et al., 2017). Both PTCH1 and HpnN contain one α+β sandwich fold in each of their extracellular or periplasmic domains, with an interrupting sequence inserted between helix 1 and strand 2 (Figures 4 and S6B).

## A Hydrophobic Conduit within PTCH1 Is Essential for Its Activity

To examine the possibility of transporter-like function, we probed for potential substrate-binding cavities in the PTCH1
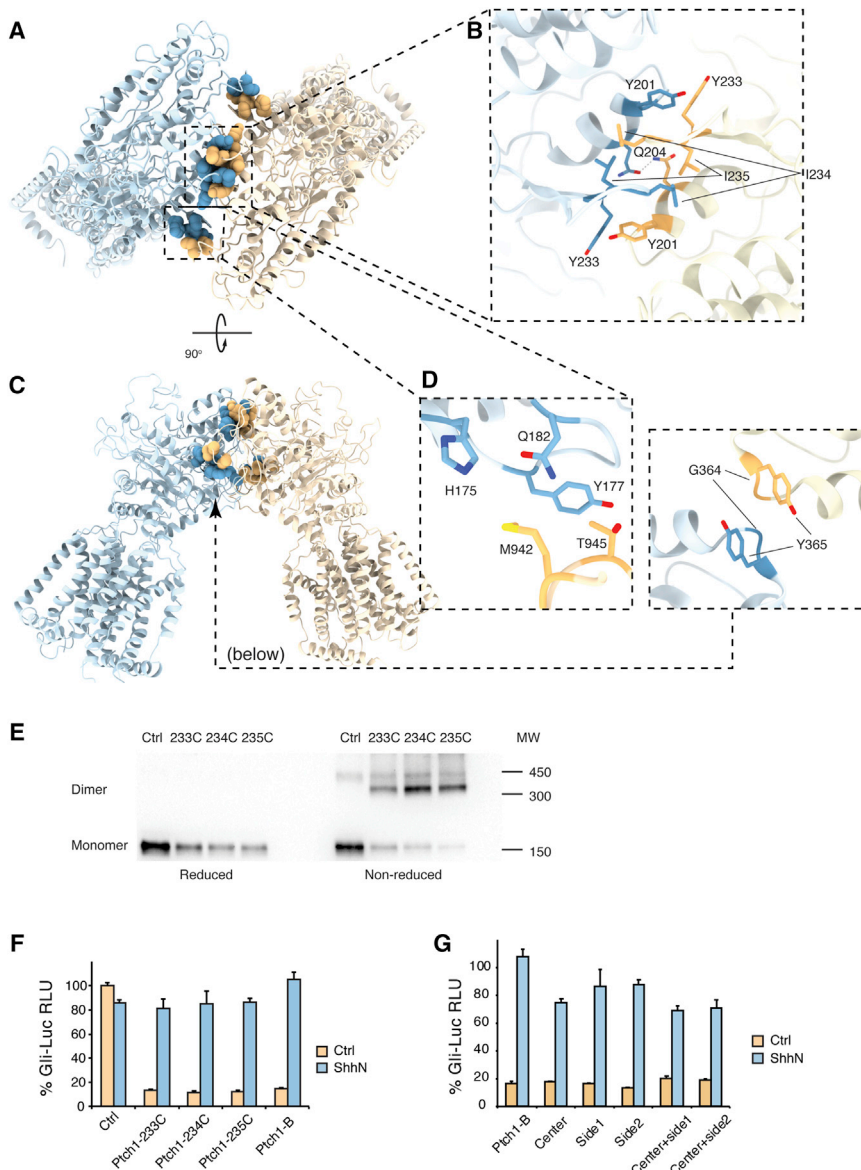
**Figure 2. Interactions at the PTCH1 Dimer Interface**

(A and B) The PTCH1 dimer interface viewed from the top (A), with a close-up view of the interacting residues Y233, L234, and L235 (B).

(C) Side view of the dimer.

(D) Enlarged views of residues on the side and the bottom that may stabilize the dimer.

(E) Western blot of HA-tagged Ptch1-B and variants carrying cysteine substitutions at the dimer interface. Under non-reducing conditions, a high-molecular-weight band corresponding to the PTCH1 dimer was seen in all cysteine variants but not Ptch1-B. This band collapsed into a monomer band under reducing conditions. The ~450-kDa band present in all non-reducing gel samples is likely due to non-specific disulfide formation during cell lysis because 14 cysteines are present on the cytosolic side of Ptch1-B. Cross-linking of the Y233C variant was less efficient than cross-linking of the I234C or I235C variants, consistent with the relative positions of these residues in the model (the distance between the Cα atoms of Y233 in the two subunits is 12 Å, farther than optimal for disulfide bond formation, whereas the distance between I234 or I235 is less than 7 Å, within optimal range for disulfide bond formation).

(F) All cysteine-substituted variants retain normal *Ptch1* activity in a Gli-dependent luciferase reporter assay in the *Ptch1*$^{-/-}$ cell line.

(G) Alterations to the dimer interface did not affect PTCH1 activity. "Center" contains Y233A, L234R, and L235R. "Side 1" contains M942A and T945A. "Side 2" contains H175A, Y177A, and Q182A. Data for each condition were averaged from triplicates, with error bars indicating SEM.

nate (CHS), a commonly used cholesterol analog, in protein purification (Figure 5C); thus, the bound molecules are likely to be CHS, cholesterol, or its cellular derivatives. These three locations outline a path similar to the substrate translocat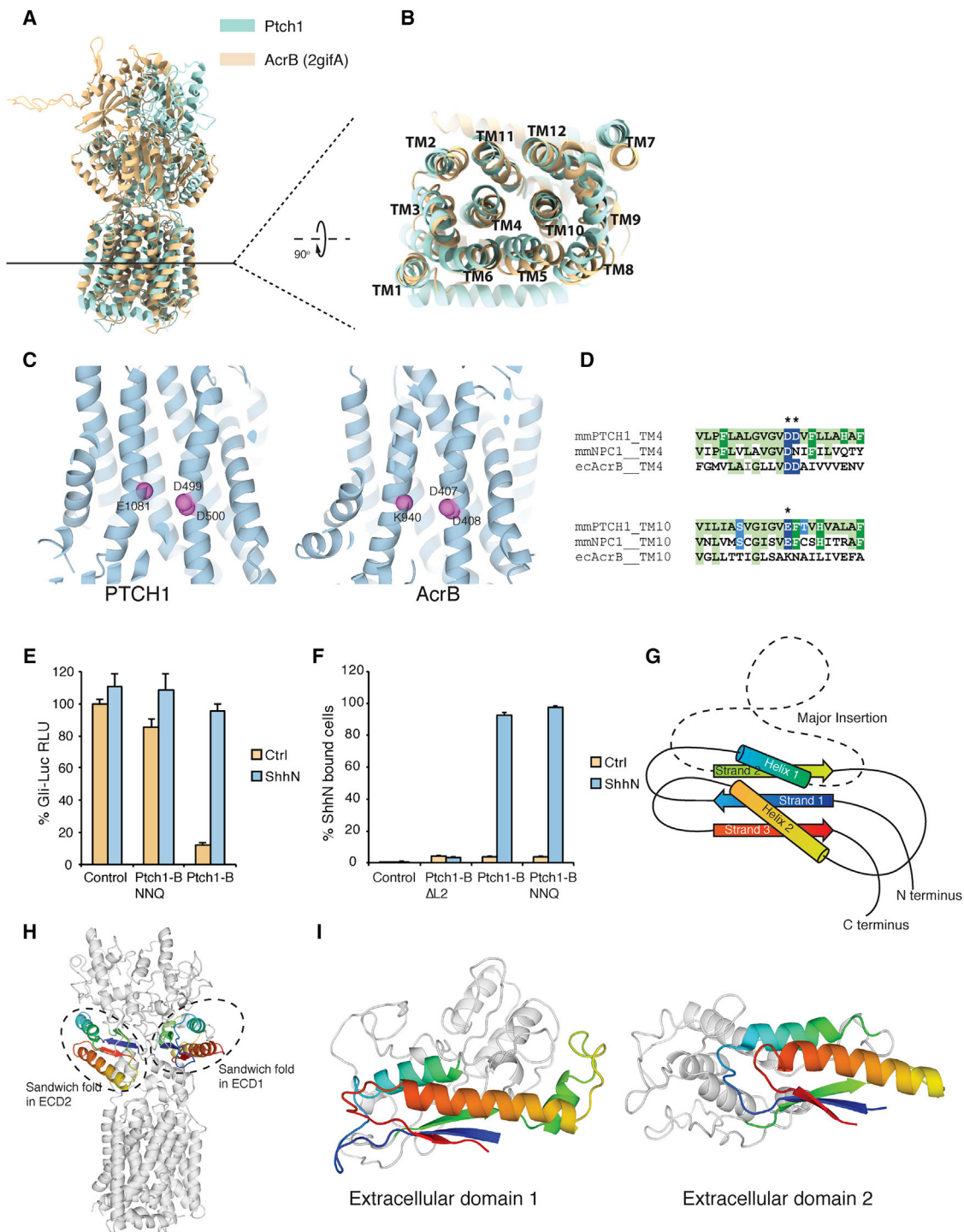ion path in HpnN, suggesting that a physiological substrate, likely structurally related to cholesterol, may be similarly bound and transported by PTCH1.

To test the potential role of this hydrophobic cavity as a conduit for transport, we introduced alterations designed to occlude it. Our efforts focused on site II because this site was included within the elongated cavity and fully enclosed by side chains of hydrophobic residues. We found, in the Gli-dependent luciferase reporter assay in *Ptch1*$^{-/-}$ MEFs described above (Figure 1A), that combined alteration of hydrophobic residues lining the conduit impaired the ability of PTCH1 to suppress SMO (Figure 5D). However, these mutations left intact its ability to bind to ShhN (Figure 5E), indicating stability and normal folding of these PTCH1 variants. Most of these alterations (highlighted in Figure 5C) substituted bulky phenylalanine residues for aliphatic residues (valine, leucine, and isoleucine), potentially blocking the substrate passage by clogging the conduit. These

structure. We found an elongated cavity that courses between the two α+β sandwich folds of the PTCH1 extracellular domain, similar to the path of a cavity in HpnN (Figure 5A). Interestingly, extra densities are apparent in three locations in high-resolution maps of PTCH1: one near the extracellular end of the cavity (site I), a second within the cavity (site II), and the third one (site III; Figure 5B) at the top of a groove between TM1 and TM2. In HpnN, a structurally homologous groove on the side of TM1 has been proposed as the substrate entry site and is continuous with the cavity in one conformation (Kumar et al., 2017). The residues surrounding these three densities seen in the PTCH1 structure are primarily hydrophobic (Figure 5C), suggesting that the bound molecules are probably hydrophobic and could be detergent or endogenous lipids carried through purification. The shape and dimension of the densities resemble those of cholesterol (Figure 5C), and we included cholesterol hemisucci-

**Figure 3. Conserved Features of PTCH1 and Other RND Family Members**

(A and B) Overlay of the PTCH1 structure model (aqua) with AcrB (wheat), shown as seen from the plane of the membrane (A) and as a section through the transmembrane domain (B). The transmembrane domains align well, whereas the extracellular or periplasmic domains diverge significantly.

(C) The key charged residues in TM4 and TM10 are shown as spheres in the cartoon representations of PTCH1 (left) and AcrB (right).

(D) The residues in (C) are highlighted (asterisk) in the sequence alignment of PTCH1, mouse NPC1, and *E. coli* AcrB.

(E and F) These charged residues are altered to generate Ptch1-B NNQ (D499N, D500N, and E1081Q). This PTCH1 variant failed to suppress basal activity in *Ptch1* $^{-/-}$ cells in a Gli-dependent luciferase assay (E) but still bound ShhN (F). Data for each condition were averaged from triplicates, with error bars indicating SEM.

*(legend continued on next page)*

observations thus support the hypothesis that a hydrophobic substrate may move through this conduit during the PTCH1 activity cycle.

## Redistribution of Membrane Cholesterol by PTCH1

As our structure suggests cholesterol transport activity for PTCH1 and cholesterol is known to be required for SMO activation (Cooper et al., 2003), we tested the effect of PTCH1 expression on cellular cholesterol distribution. We recently developed techniques to directly measure cholesterol activity in the membrane utilizing a set of sensors derived from the cholesterol-binding domain of Perfringolysin O (PFO), each with a distinct affinity for cholesterol and covalently labeled with a unique solvatochromic fluorophore (Liu et al., 2017; STAR Methods). The fluorescence emission of these sensors shifts upon interaction with membrane cholesterol (Figure 6A), permitting ratiometric quantification of cholesterol activity in cellular membranes. The use of a pair of spectrally orthogonal sensors, one microinjected into cells and the other added to the extracellular medium, permits simultaneous *in situ* measurement of cholesterol activity in the inner leaflet (IPM) and the outer leaflet (OPM) of the plasma membrane. Using these approaches, we recently found that the chemical activity of cholesterol in the plasma membrane is distinct across the bilayer, with a level of sensor-accessible cholesterol 10- to 15-fold higher in OPM compared with IPM in many cell types (Liu et al., 2017), including the HEK293 cells used for our studies here.

We assayed the effect of PTCH1 on cholesterol distribution in HEK293 cells by transfection with constructs for expression of Ptch1-B or Ptch1-B variants. As reported previously, the spatially averaged IPM cholesterol activity in mock-transfected cells corresponded to about 3 mol % compared with 43 mol % cholesterol activity in OPM (Figure 6B). Cells transfected for expression of Ptch1-B exhibited a bimodal distribution of IPM cholesterol activity, with IPM cholesterol activity reduced below the detection limit of the sensor in approximately half of the cells (Figures 6B and 6C; entire cell population in Figure S7A). Cells expressing the Ptch1-B-NNQ variant (an inactive PTCH1 variant; Figure 3E) or the Ptch1-B-IVL variant with the conduit blocked (I766F, V111F, L114F; the inactive PTCH1 variant shown in Figure 5D), in contrast, showed little change in IPM cholesterol activity compared with mock-transfected cells (Figure 6B). The bimodal distribution in IPM cholesterol activity in Ptch1-B-transfected cells is likely due to transfection efficiency being limited to around half of the cells.

We then found, upon addition of purified ShhN ligand to inactivate Ptch1-B and quantification at 0, 1, 2, 3, 4, 5, and 10 min (Figure 6D), that IPM cholesterol activity was restored to normal levels within 5 min (Figure 6E). The increase in IPM cholesterol activity was synchronized with a comparable reduction in OPM cholesterol activity (Figure S7B), suggesting that the cholesterol changes observed upon inactivation of PTCH1 by ShhN might result from cross-bilayer redistribution.

To provide a direct indication of Ptch1-B expression, we used blue fluorescent protein (BFP)-tagged Ptch1-B variants; with these variants, only IPM cholesterol can be measured because of spectral overlap of BFP with the OPM cholesterol sensor. IPM cholesterol activity in BFP-Ptch1-B-expressing cells was nearly identical to that of the subpopulation of untagged Ptch1-B-transfected cells, showing drastically lowered IPM cholesterol activity (Figure 6E). Furthermore, the hydrophobic cavity mutant of Ptch1-B (BFP-tagged or untagged) caused neither the reduction of IPM cholesterol in resting cells nor its increase in response to ShhN (Figure 6E), demonstrating the importance of an intact hydrophobic conduit for the effects of Ptch1-B on reduction of IPM cholesterol activity. In addition, we found that IPM cholesterol activity in $Ptch1^{-/-}$ MEFs was similarly reduced by transfection for expression of BFP-tagged Ptch1-B and that ShhN stimulation reversed this change without affecting IPM cholesterol of the control $Ptch1^{-/-}$ MEFs (Figure 6F). Full-length PTCH1 produced essentially the same effect on IPM cholesterol and response to ShhN stimulation as Ptch1-B in this assay (Figure 6F). We also noted a correlation between Ptch1-B expression and the reduction in IPM cholesterol activity, with a greater reduction in IPM cholesterol activity at higher transfection doses (Figure S7C). This correlation of Ptch1-B expression level with IPM cholesterol effect and its rapid reversal by ShhN together suggest that PTCH1 likely acts directly to maintain reduced IPM cholesterol activity.

We sought to further strengthen the link between the PTCH1 effect on IPM cholesterol activity and SMO regulation by comparing the levels of PTCH1 required for IPM cholesterol activity reduction and for SMO suppression. Endogenous PTCH1 is localized in the primary cilium, where it regulates SMO and receives the Hedgehog ligand (Rohatgi et al., 2007), but no sensor is available for ciliary membrane cholesterol measurements. We therefore compared PTCH1 protein levels in the plasma membrane in our cholesterol assays with the levels of endogenous or transfected PTCH1 in cilia. In the first such experiment, we measured the mean plasma membrane fluorescence intensity of Ptch1-B-BFP transfected into $Ptch1^{-/-}$ MEFs under conditions for cholesterol quantification and compared it with the fluorescence intensity in the primary cilium of cells transfected at a dose that permits ShhN-induced transcriptional response with a Gli-dependent luciferase reporter. We found that the mean intensity under the conditions of cholesterol quantification is similar to the mean intensity of the primary cilium under conditions of the luciferase assay (Figure S7D), supporting a correspondence between the effect of PTCH1 on IPM cholesterol and its ability to suppress SMO.

As an independent approach, we also estimated the levels of PTCH1 protein in the ciliary membrane of untransfected 3T3

---

(G) Schematic view of the conserved α-β sandwich fold present within the extracellular, periplasmic, or lumenal domains of RND family proteins. Structural elements are colored in spectral sequence from N to C termini (blue to red, respectively), with a common site of non-conserved sequence insertion shown as a dashed line.

(H) PTCH1 structure highlighting the two α+β sandwich folds in the extracellular domain.

(I) Enlarged view of the sandwich folds in ECD1 (left) and ECD2 (right). The sandwich fold is colored as in (G), with inserted sequences shown in gray.
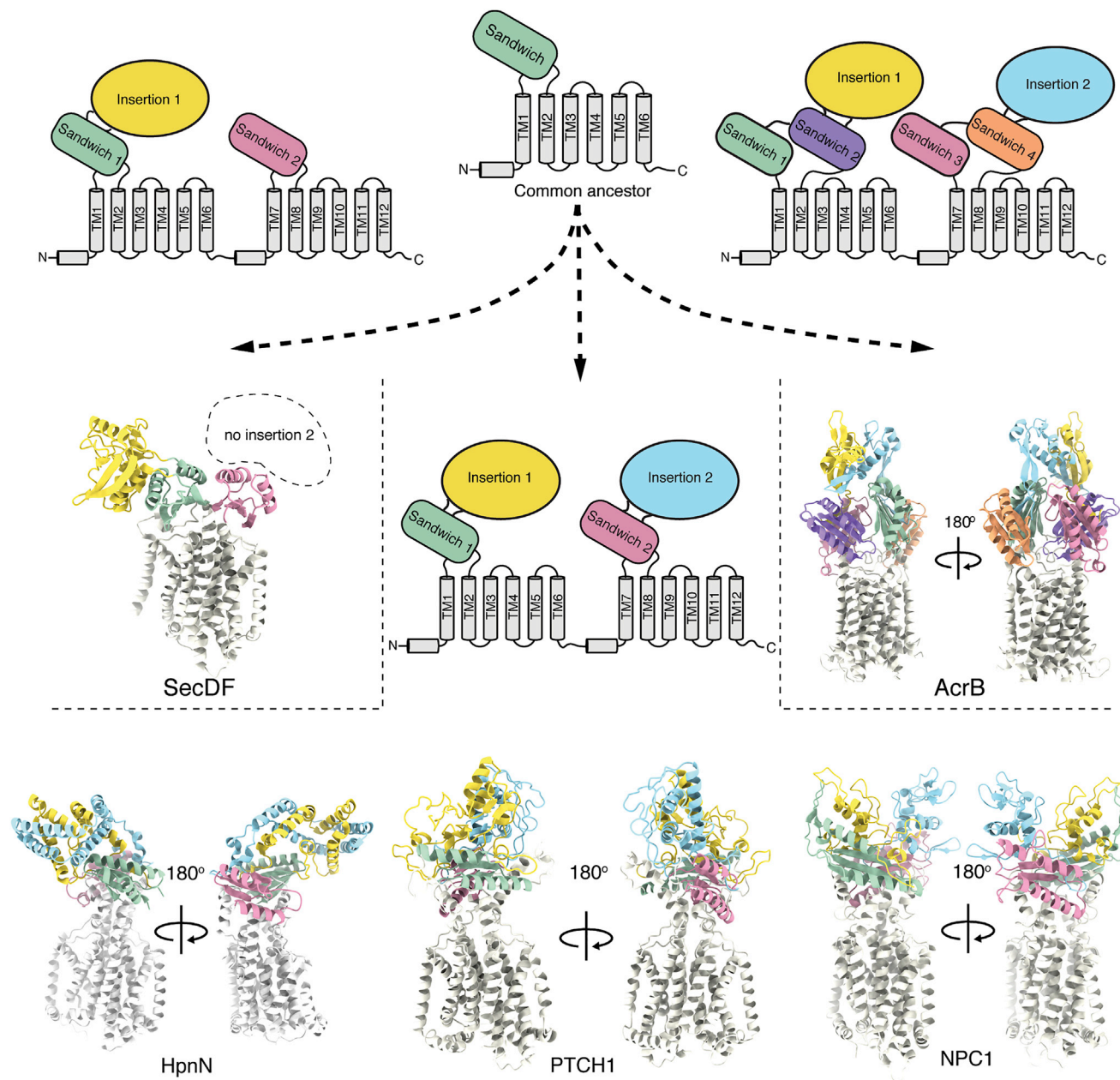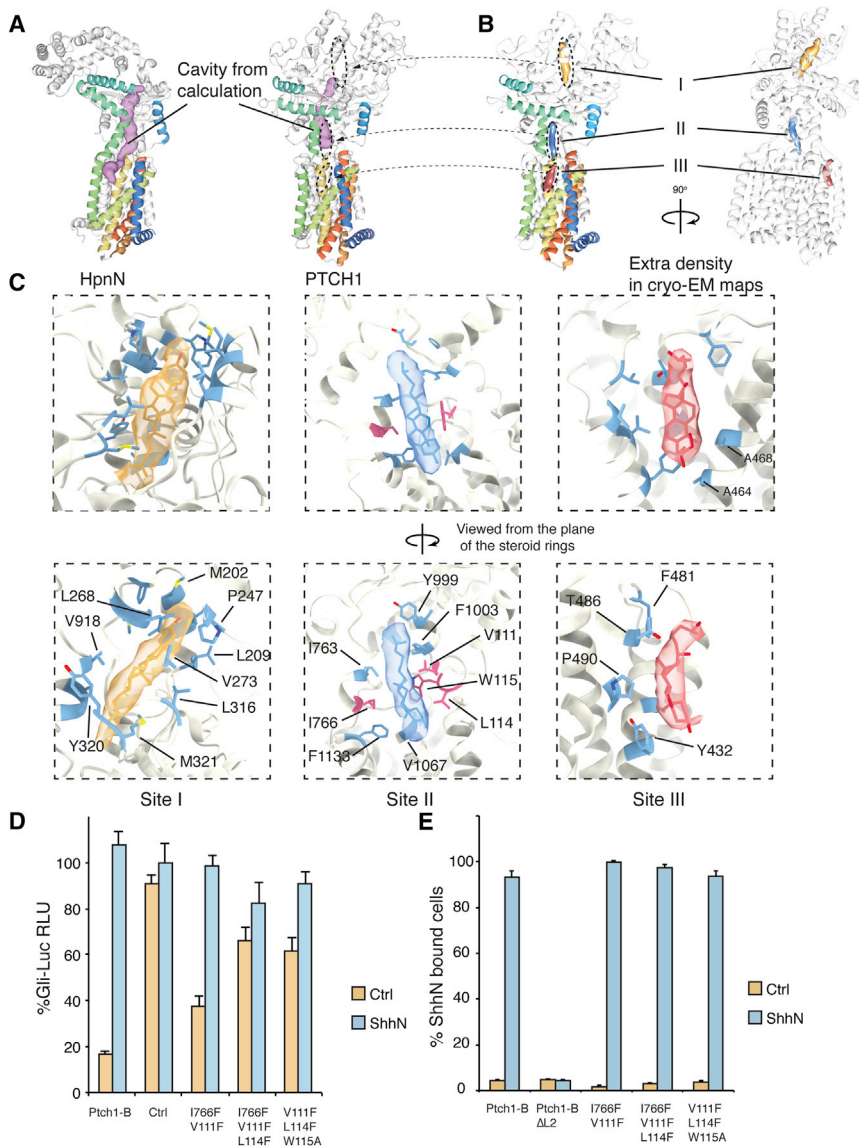
**Figure 4. Potential Evolutionary Derivation of Various RND Transporters**

The ancestral RND progenitor most likely comprised 6 TM helices with one sandwich fold inserted between TM1 and TM2. Duplication of the entire progenitor led to a 12 TM structure. Before or after this duplication, an insertion into the sandwich fold imparted diverse functions, as shown for SecDF, HpnN, NPC1, and PTCH1. In AcrB, duplication of the sandwich fold likely preceded duplication of the 6 TM progenitor, giving rise to a total of 4 sandwich folds.

cells and in the plasma membrane of transfected *Ptch1*$^{-/-}$ MEFs by measuring the fluorescence intensity of fluorescently labeled ShhN bound to PTCH1. We found that the mean fluorescence intensity of ShhN binding to the surface of transfected cells was around twice that of the ciliary membrane of 3T3 cells (Figure S7E). This quantification suggests that the plasma membrane concentration of PTCH1 used in our cholesterol assay is within the physiological range of PTCH1 in the primary cilium.

Collectively, these measurements of PTCH1 expression levels support the model that PTCH1 suppresses SMO by reducing IPM cholesterol activity under physiologic conditions (Figure 6G). This model is further supported by the simultaneous loss of SMO suppression and IPM cholesterol activity of altered forms of PTCH1, including the NNQ-charged triad mutant and the IVL conduit-clogging mutant and coordinate reversal of SMO suppression and the IPM cholesterol effect by ShhN-mediated inactivation of PTCH1. In this model,

**Figure 5. Potential Path for Lipidic Substrate Transport in PTCH1**

(A) Comparison of extracellular or periplasmic domain cavities in PTCH1 and the HpnN hopanoid transporter of *Burkholderia multivorans*. Both cavities are similarly positioned, but the HpnN cavity extends further downward to open to the side of the transmembrane domain. Cavities were calculated using the Caver program.

(B) Three discrete regions of extra density located within (II) and at the ends (I and III) of the PTCH1 cavity are present in high-resolution maps. In HpnN, the periplasmic cavity extends to the side of TM1 and is proposed to receive substrates for transport to the outer membrane. Densities I, II, and III outline a potential substrate translocation path similar to that in HpnN.

(C) Hydrophobic residues surrounding densities I, II, and III favor interactions with hydrophobic substrates. A model of cholesterol is placed inside each density as a reference.

(D and E) Combinations of altered residues highlighted in red in (C) impaired the ability of PTCH1 to suppress basal activity in *Ptch1*$^{-/-}$ cells in a Gli-dependent luciferase assay (D) but maintained ShhN binding (E). Data for each condition were averaged from triplicates, with error bars indicating SEM.

Interestingly, when this hydrophobic extension is added as an acyl chain *in vitro*, the degree of Hedgehog signaling activity correlates positively with the length of the acyl chain (Pepinsky et al., 1998). We speculate that the N-terminal hydrophobic extension may be positioned to occlude the hydrophobic conduit, with improved signaling ability correlating with longer acyl chain lengths because of improved blockade. We note that, in two of the published structures of PTCH1 in complex with palmitoylated ShhN, the N-terminal hydrophobic extension occupies the conduit containing density II (Qi et al., 2018a, 2018b).

## DISCUSSION

The structure of PTCH1 is consistent with the proposed hypothesis that PTCH1 functions as an RND-like transporter to control access of modulatory ligands to SMO (Taipale et al., 2002). The striking similarity in the transmembrane domain between PTCH1 and bacterial RND homologs and the requirement of a charged triad for PTCH1 activity together suggest that PTCH1 may be capable of harnessing energy from ions flowing down an electrochemical gradient to drive conformational switching.

Although the PTCH1 extracellular domain differs significantly from that of the well-characterized bacterial transporter AcrB, the cavity positioned between sandwich domains in PTCH1, HpnN, and NPC1 is similar, suggesting a potentially similar
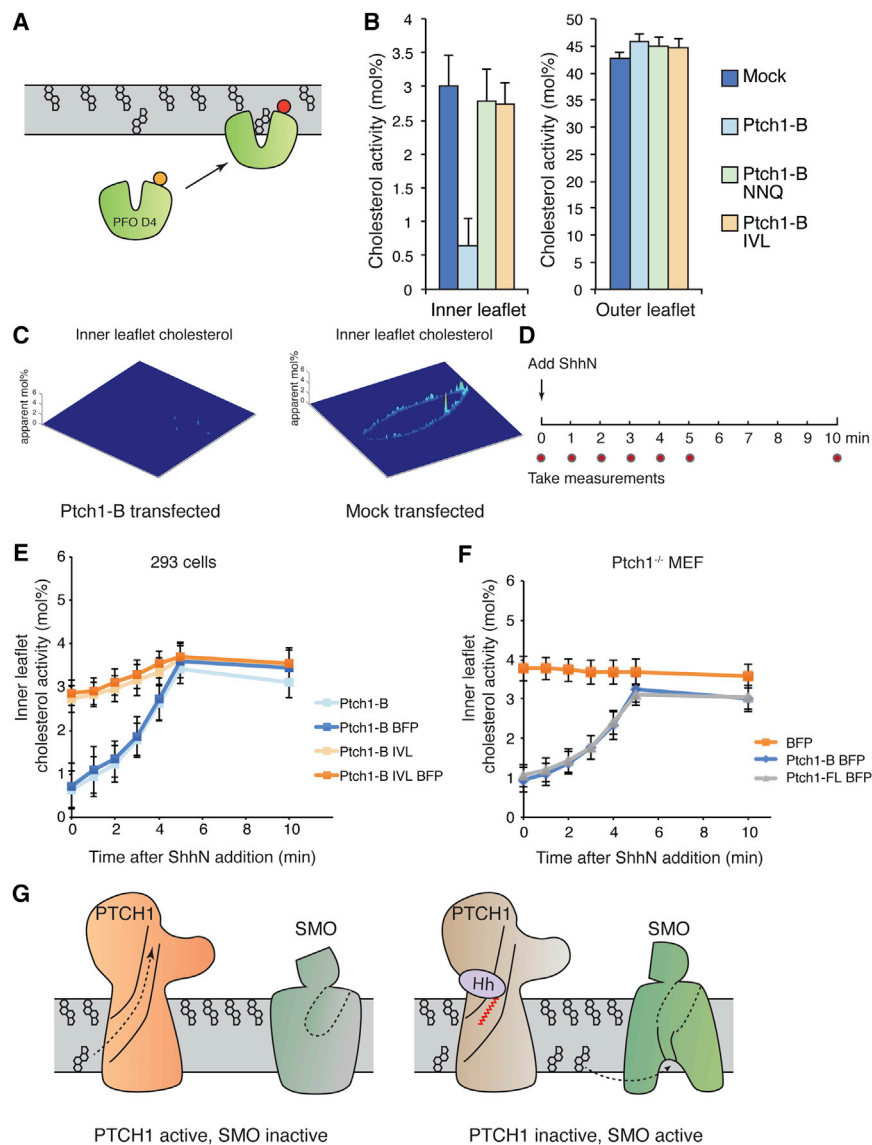
Hedgehog binding to PTCH1 would inhibit the transport process, resulting in a return to normal of IPM cholesterol activity and consequent SMO activation. Consistent with this model, recent structural work shows that SMO in its active conformation contains a tunnel opening to the inner leaflet of the membrane (Huang et al., 2018), potentially correlating with increased IPM cholesterol activity. Furthermore, *in vitro* reconstitution of purified Smoothened protein demonstrates that its activity can be switched on by cholesterol levels in the range of IPM cholesterol measured here upon Patched inactivation (Myers et al., 2017), and recent evidence suggests a possible sterol binding site at the inner leaflet level of the SMO TM domain (Raleigh et al., 2018).

It is noteworthy that Hedgehog protein signaling activity, but not affinity of receptor binding, depends on a hydrophobic extension from its amino terminus, usually accomplished *in vivo* by palmitoylation (Chamoun et al., 2001; Pepinsky et al., 1998).

**Figure 6. PTCH1 Alters Cellular Cholesterol Distribution in the Plasma Membrane**

(A) Schematic diagram of the cholesterol sensor. The cholesterol-binding D4 domain from PFO was engineered and modified with a solvatochromatic fluorophore so that its fluorescence emission shifts upon binding to cholesterol in the plasma membrane. This engineered sensor provides a ratiometric readout for cholesterol activity in the outer leaflet or the inner leaflet (with cell microinjection) of the plasma membrane.

(B) The cholesterol activity of the inner (IPM) and outer leaflets (OPM) is compared in the bar graph. The mock-transfected cells or cells transfected with Ptch1-B harboring alterations to the charged triad in the transmembrane domain (NNQ) or blocking mutations in the transport conduit (I766F, V111F, L114F [IVL]), showed similar levels of inner and outer leaflet cholesterol activity. In contrast, in Ptch1-B-transfected cells, the population with lower cholesterol activity (approximately half of the total cells measured, as in Figure S7A) showed a dramatic reduction in inner leaflet cholesterol activity, whereas the outer leaflet cholesterol activity was largely unchanged. For mock-transfected cells, Ptch1-B, and Ptch1-B NNQ, n = 20; for Ptch1-B IVL, n = 10. Cholesterol activity is derived from spatially averaged sensor readout.

(C) Inner leaflet cholesterol content of representative cells. Note that, in Ptch1-B-expressing cells, inner leaflet cholesterol activity was reduced below the detection limit of our IPM sensor.

(D) 293 cells expressing Ptch1-B variants were stimulated with ShhN, and cholesterol activity was measured at intervals before and after purified ShhN (C25II) treatment.

(E) Changes in IPM cholesterol activity in 293 cells after addition of ShhN. In the subset of Ptch1-B-transfected cells with low IPM cholesterol activity, ShhN restored IPM cholesterol activity to control levels within 5 min. In cells expressing the Ptch1-B variant harboring blocking mutations in the transport conduit (IVL), IPM cholesterol activity was within the normal range and did not change in response to ShhN. When BFP-tagged Ptch1-B variants were used to give a direct indication of Ptch1-B expression, the change in IPM choles-

terol activity was similar to that seen with untagged Ptch1-B. Ptch1-B had a sample size of 20, Ptch1-B IVL had a sample size of 10, and BFP-tagged variants had a sample size of 10.

(F) The effect of PTCH1 variants on IPM cholesterol activity was tested in *Ptch1*$^{-/-}$ MEFs. BFP-tagged Ptch1-B variants were used to provide a direct indication of PTCH1 expression. BFP alone did not cause any reduction in IPM cholesterol activity or increase after ShhN addition. Both Ptch1-B and full-length PTCH1 reduced IPM cholesterol activity, and the change was reversed upon addition of ShhN. Under all conditions, n = 10.

(G) Model for PTCH1-SMO regulation. PTCH1 may transport inner leaflet cholesterol out of the membrane and thus maintain SMO quiescence. Upon binding to PTCH1, the N-terminal hydrophobic extension of ShhN occludes the hydrophobic conduit in PTCH1 and blocks PTCH1 transport function. Increased inner leaflet cholesterol then leads to SMO activation.

Error bars indicate SEM.

transport mechanism. The possibility that HpnN may transport hopanoids (Doughty et al., 2011), bacterial lipids with sterol-like rigid rings, along with its sequence similarity to PTCH1 led to the proposal that PTCH1 might originate from HpnN in evolution (Hausmann et al., 2009). In addition, NPC1 is proposed to be a cholesterol transporter and is required for efflux of lysosomal cholesterol. The conduit in NPC1 thus may also be utilized for cholesterol transport, but apparently in the opposite direction,

in which cholesterol moves from the lumenal domain into the membrane.

In the Hedgehog signaling pathway, cholesterol is required to activate SMO (Cooper et al., 2003), the downstream target of PTCH1. A previous study (Bidet et al., 2011) reported that Patched expression in yeast cells increased extrusion of a fluorescent boron dipyromethanene sterol derivative (BOD-IPY-cholesterol) into the external medium by 2-fold.

Interpretation of this study, however, is unclear because significant amounts of BODIPY-cholesterol were spontaneously released into the medium without PTCH1 expression, whereas spontaneous release of cholesterol into aqueous medium is implausible without an acceptor. Our direct measurements of endogenous cholesterol in the membrane and the presence in our PTCH1 structure of cholesterol-like densities within and at either end of a hydrophobic conduit together constitute strong evidence that PTCH1 may function in cholesterol transport.

Nevertheless, some questions remain. Although PTCH1 appears to alter inner leaflet cholesterol in cells, the extra density present in the transmembrane domain is located at the level of the outer leaflet of the membrane. This observation may be accounted for by different dwell times of substrate along the transport path. Inner leaflet cholesterol may move outward along a shallow groove present between TM1 and TM2 but remain longer at the level of the outer leaflet because of higher affinity for that site prior to entry into the extracellular conduit. In addition, cholesterol is insoluble in water and would require a sink for export. HpnN delivers lipidic substrates directly to the outer membrane, and NPC1 apparently receives cholesterol from NPC2, a lipid-carrying partner. Because eukaryotic cells lack an outer membrane, PTCH1 export of a cholesterol-like lipid may require a lipid carrier as the sink, suggesting the possible existence of an unidentified lipid carrier protein that partners with PTCH1. Finally, it seems unlikely that PTCH1, under physiological conditions, would alter the cholesterol distribution of the entire plasma membrane because PTCH1 is normally localized to the primary cilium (Corbit et al., 2005; Kim et al., 2015; Rohatgi et al., 2007). Given the presence of a distinct ionic and membrane environment in the primary cilium (Chávez et al., 2015; DeCaen et al., 2013; Garcia-Gonzalo et al., 2015; Raleigh et al., 2018), PTCH1 activity may differ from that in the plasma membrane; more refined measurements might be possible with future availability of a sensor for ciliary membrane cholesterol.

PTCH1 clearly affects IPM cholesterol activity, but we have not yet biochemically reconstituted cholesterol transport, which may require incorporation of an unidentified cholesterol acceptor. Nevertheless, our data limit the conceivable modes of indirect PTCH1 action on cholesterol, leaving direct action as the simplest explanation of our findings. Reversal of PTCH1-mediated reduction in IPM cholesterol activity begins immediately and is completed within minutes of ShhN addition. PTCH1-regulated transcriptional and translational events are unlikely to generate a sufficient effect to account for the observed change within this time frame. In addition, the NNQ and IVL residues altered in inactive mutated forms of PTCH1 are internal, making their participation in an interaction between PTCH1 and a protein partner unlikely. PTCH1 action on a non-cholesterol lipid, however, remains a possibility because the change in our sensor readout may arise from a change in availability of cholesterol through indirect effects on a lipid that forms a complex with cholesterol (Das et al., 2014). Given the sterol-like densities present in and near the essential hydrophobic conduit in our PTCH1 structure, however, the PTCH1 substrate seems likely to be a sterol, and cholesterol redistribution is the most parsimonious interpretation of our observations that links PTCH1 activity to SMO regulation.

## STAR★METHODS

Detailed methods are provided in the online version of this paper and include the following:

- KEY RESOURCES TABLE
- CONTACT FOR REAGENT AND RESOURCE SHARING
- EXPERIMENTAL MODEL AND SUBJECT DETAILS
- METHOD DETAILS
  - Molecular cloning
  - PTCH1 purification
  - Multiangle light scattering
  - Purification of Shh variants
  - Biotinylation of purified ShhN protein
  - Preparation of Shh affinity resin
  - Shh affinity purification
  - Cryo-EM sample preparation
  - Cryo-EM Data aquisition
  - Image processing
  - Multi-body Refinement
  - Structure modeling
  - *In vitro* ShhN binding assay
  - FACS-based ShhN binding assay
  - Gli-dependent luciferase assay
  - Cellular cholesterol measurement
- QUANTIFICATION AND STATISTICAL ANALYSIS
- DATA AND SOFTWARE AVAILABILITY

### SUPPLEMENTAL INFORMATION

Supplemental Information includes seven figures, one table, and one video and can be found with this article online at https://doi.org/10.1016/j.cell.2018.10.026.

### AUTHOR CONTRIBUTIONS

Y.Z., D.P.B., Y.X., K.J.R., D.E.A., A.S., B.R.M., W.C., Y.C., and P.A.B. conceived the project and were involved in revising and editing the manuscript. Y.Z. purified PTCH1 in complex with ShhN protein variants and performed the *in vitro* characterizations. Y.Z. and K.J.R. performed Gli-luciferase assays and ShhN binding assays on the cell surface. D.P.B., Y.Z., and D.E.A. performed cryo-EM data processing. A.S. optimized the cholesterol probe.

## REFERENCES

Afonine, P.V., Grosse-Kunstleve, R.W., Echols, N., Headd, J.J., Moriarty, N.W., Mustyakimov, M., Terwilliger, T.C., Urzhumtsev, A., Zwart, P.H., and Adams, P.D. (2012). Towards automated crystallographic structure refinement with phenix.refine. Acta Crystallogr. D Biol. Crystallogr. *68*, 352–367.

Bai, X.C., Rajendra, E., Yang, G., Shi, Y., and Scheres, S.H. (2015). Sampling the conformational space of the catalytic subunit of human γ-secretase. eLife *4*, e11182.

Bidet, M., Joubert, O., Lacombe, B., Ciantar, M., Nehmé, R., Mollat, P., Brétillon, L., Faure, H., Bittman, R., Ruat, M., and Mus-Veteau, I. (2011). The hedgehog receptor patched is involved in cholesterol transport. PLoS ONE *6*, e23834.

Byrne, E.F.X., Sircar, R., Miller, P.S., Hedger, G., Luchetti, G., Nachtergaele, S., Tully, M.D., Mydock-McGrane, L., Covey, D.F., Rambo, R.P., et al. (2016). Structural basis of Smoothened regulation by its extracellular domains. Nature *535*, 517–522.

Chamoun, Z., Mann, R.K., Nellen, D., von Kessler, D.P., Bellotto, M., Beachy, P.A., and Basler, K. (2001). Skinny hedgehog, an acyltransferase required for palmitoylation and activity of the hedgehog signal. Science *293*, 2080–2084.

Chávez, M., Ena, S., Van Sande, J., de Kerchove d'Exaerde, A., Schurmans, S., and Schiffmann, S.N. (2015). Modulation of Ciliary Phosphoinositide Content Regulates Trafficking and Sonic Hedgehog Signaling Output. Dev. Cell *34*, 338–350.

Chen, Y., and Struhl, G. (1996). Dual roles for patched in sequestering and transducing Hedgehog. Cell *87*, 553–563.

Chiang, C., Litingtung, Y., Lee, E., Young, K.E., Corden, J.L., Westphal, H., and Beachy, P.A. (1996). Cyclopia and defective axial patterning in mice lacking Sonic hedgehog gene function. Nature *383*, 407–413.

Cleveland, T.E., 4th, McCabe, J.M., and Leahy, D.J. (2014). Detergent-solubilized Patched purified from Sf9 cells fails to interact strongly with cognate Hedgehog or lhog homologs. Protein Expr. Purif. *104*, 92–102.

Constantine, M., Liew, C.K., Lo, V., Macmillan, A., Cranfield, C.G., Sunde, M., Whan, R., Graham, R.M., and Martinac, B. (2016). Heterologously-expressed and Liposome-reconstituted Human Transient Receptor Potential Melastatin 4 Channel (TRPM4) is a Functional Tetramer. Sci. Rep. *6*, 19352.

Cooper, M.K., Wassif, C.A., Krakowiak, P.A., Taipale, J., Gong, R., Kelley, R.I., Porter, F.D., and Beachy, P.A. (2003). A defective response to Hedgehog signaling in disorders of cholesterol biosynthesis. Nat. Genet. *33*, 508–513.

Corbit, K.C., Aanstad, P., Singla, V., Norman, A.R., Stainier, D.Y., and Reiter, J.F. (2005). Vertebrate Smoothened functions at the primary cilium. Nature *437*, 1018–1021.

Das, A., Brown, M.S., Anderson, D.D., Goldstein, J.L., and Radhakrishnan, A. (2014). Three pools of plasma membrane cholesterol and their relation to cholesterol homeostasis. eLife *3*, e02882.

DeCaen, P.G., Delling, M., Vien, T.N., and Clapham, D.E. (2013). Direct recording and molecular identification of the calcium channel of primary cilia. Nature *504*, 315–318.

Dessaud, E., McMahon, A.P., and Briscoe, J. (2008). Pattern formation in the vertebrate neural tube: a sonic hedgehog morphogen-regulated transcriptional network. Development *135*, 2489–2503.

Doughty, D.M., Coleman, M.L., Hunter, R.C., Sessions, A.L., Summons, R.E., and Newman, D.K. (2011). The RND-family transporter, HpnN, is required for hopanoid localization to the outer membrane of Rhodopseudomonas palustris TIE-1. Proc. Natl. Acad. Sci. USA *108*, E1045–E1051.

Emsley, P., Lohkamp, B., Scott, W.G., and Cowtan, K. (2010). Features and development of Coot. Acta Crystallogr. D Biol. Crystallogr. *66*, 486–501.

Fuse, N., Maiti, T., Wang, B., Porter, J.A., Hall, T.M., Leahy, D.J., and Beachy, P.A. (1999). Sonic hedgehog protein signals not as a hydrolytic enzyme but as an apparent ligand for patched. Proc. Natl. Acad. Sci. USA *96*, 10992–10999.

Garcia-Gonzalo, F.R., Phua, S.C., Roberson, E.C., Garcia, G., 3rd, Abedin, M., Schurmans, S., Inoue, T., and Reiter, J.F. (2015). Phosphoinositides Regulate Ciliary Protein Trafficking to Modulate Hedgehog Signaling. Dev. Cell *34*, 400–409.

Gerling, M., Büller, N.V., Kirn, L.M., Joost, S., Frings, O., Englert, B., Bergström, Å., Kuiper, R.V., Blaas, L., Wielenga, M.C., et al. (2016). Stromal Hedgehog signalling is downregulated in colon cancer and its restoration restrains tumour growth. Nat. Commun. *7*, 12321.

Goddard, T.D., Huang, C.C., Meng, E.C., Pettersen, E.F., Couch, G.S., Morris, J.H., and Ferrin, T.E. (2018). UCSF ChimeraX: Meeting modern challenges in visualization and analysis. Protein Sci. *27*, 14–25.

Gong, X., Qian, H., Cao, P., Zhao, X., Zhou, Q., Lei, J., and Yan, N. (2018). Structural basis for the recognition of Sonic Hedgehog by human Patched1. Science *361*, eaas8935.

Goodrich, L.V., Milenković, L., Higgins, K.M., and Scott, M.P. (1997). Altered neural cell fates and medulloblastoma in mouse patched mutants. Science *277*, 1109–1113.

Hausmann, G., von Mering, C., and Basler, K. (2009). The hedgehog signaling pathway: where did it come from? PLoS Biol. *7*, e1000146.

Huang, P., Nedelcu, D., Watanabe, M., Jao, C., Kim, Y., Liu, J., and Salic, A. (2016). Cellular Cholesterol Directly Activates Smoothened in Hedgehog Signaling. Cell *166*, 1176–1187.e14.

Huang, P., Zheng, S., Wierbowski, B.M., Kim, Y., Nedelcu, D., Aravena, L., Liu, J., Kruse, A.C., and Salic, A. (2018). Structural Basis of Smoothened Activation in Hedgehog Signaling. Cell *174*, 312–324.e6.

Ilca, S.L., Kotecha, A., Sun, X., Poranen, M.M., Stuart, D.I., and Huiskonen, J.T. (2015). Localized reconstruction of subunits from electron cryomicroscopy images of macromolecular complexes. Nat. Commun. *6*, 8843.

Ingham, P.W. (1993). Localized hedgehog activity controls spatial limits of wingless transcription in the Drosophila embryo. Nature *366*, 560–562.

Ingham, P.W., and McMahon, A.P. (2001). Hedgehog signaling in animal development: paradigms and principles. Genes Dev. *15*, 3059–3087.

Ingham, P.W., Taylor, A.M., and Nakano, Y. (1991). Role of the Drosophila patched gene in positional signalling. Nature *353*, 184–187.

Johnson, R.L., Rothman, A.L., Xie, J., Goodrich, L.V., Bare, J.W., Bonifas, J.M., Quinn, A.G., Myers, R.M., Cox, D.R., Epstein, E.H., Jr., and Scott, M.P. (1996). Human homolog of patched, a candidate gene for the basal cell nevus syndrome. Science *272*, 1668–1671.

Kawate, T., and Gouaux, E. (2006). Fluorescence-detection size-exclusion chromatography for precrystallization screening of integral membrane proteins. Structure *14*, 673–681.

Kim, J., Kato, M., and Beachy, P.A. (2009). Gli2 trafficking links Hedgehog-dependent activation of Smoothened in the primary cilium to transcriptional activation in the nucleus. Proc. Natl. Acad. Sci. USA *106*, 21666–21671.

Kim, J., Hsia, E.Y., Brigui, A., Plessis, A., Beachy, P.A., and Zheng, X. (2015). The role of ciliary trafficking in Hedgehog receptor signaling. Sci. Signal. *8*, ra55.

Koronakis, V., Sharff, A., Koronakis, E., Luisi, B., and Hughes, C. (2000). Crystal structure of the bacterial membrane protein TolC central to multidrug efflux and protein export. Nature *405*, 914–919.

Kumar, N., Su, C.C., Chou, T.H., Radhakrishnan, A., Delmar, J.A., Rajashankar, K.R., and Yu, E.W. (2017). Crystal structures of the *Burkholderia multivorans* hopanoid transporter HpnN. Proc. Natl. Acad. Sci. USA *114*, 6557–6562.

Lee, J.J., Perera, R.M., Wang, H., Wu, D.C., Liu, X.S., Han, S., Fitamant, J., Jones, P.D., Ghanta, K.S., Kawano, S., et al. (2014). Stromal response to Hedgehog signaling restrains pancreatic cancer progression. Proc. Natl. Acad. Sci. USA 111, E3091–E3100.

Lee, J.J., Rothenberg, M.E., Seeley, E.S., Zimdahl, B., Kawano, S., Lu, W.J., Shin, K., Sakata-Kato, T., Chen, J.K., Diehn, M., et al. (2016). Control of inflammation by stromal Hedgehog pathway activation restrains colitis. Proc. Natl. Acad. Sci. USA 113, E7545–E7553.

Li, X., Saha, P., Li, J., Blobel, G., and Pfeffer, S.R. (2016). Clues to the mechanism of cholesterol transfer from the structure of NPC1 middle lumenal domain bound to NPC2. Proc. Natl. Acad. Sci. USA 113, 10079–10084.

Liu, S.L., Sheng, R., O'Connor, M.J., Cui, Y., Yoon, Y., Kurilova, S., Lee, D., and Cho, W. (2014). Simultaneous in situ quantification of two cellular lipid pools using orthogonal fluorescent sensors. Angew. Chem. Int. Ed. Engl. 53, 14387–14391.

Liu, S.L., Sheng, R., Jung, J.H., Wang, L., Stec, E., O'Connor, M.J., Song, S., Bikkavilli, R.K., Winn, R.A., Lee, D., et al. (2017). Orthogonal lipid sensors identify transbilayer asymmetry of plasma membrane cholesterol. Nat. Chem. Biol. 13, 268–274.

Lu, X., Liu, S., and Kornberg, T.B. (2006). The C-terminal tail of the Hedgehog receptor Patched regulates both localization and turnover. Genes Dev. 20, 2539–2551.

Luchetti, G., Sircar, R., Kong, J.H., Nachtergaele, S., Sagner, A., Byrne, E.F., Covey, D.F., Siebold, C., and Rohatgi, R. (2016). Cholesterol activates the G-protein coupled receptor Smoothened to promote Hedgehog signaling. eLife 5, e20304.

McLellan, J.S., Zheng, X., Hauk, G., Ghirlando, R., Beachy, P.A., and Leahy, D.J. (2008). The mode of Hedgehog binding to Ihog homologues is not conserved across different phyla. Nature 455, 979–983.

Myers, B.R., Sever, N., Chong, Y.C., Kim, J., Belani, J.D., Rychnovsky, S., Bazan, J.F., and Beachy, P.A. (2013). Hedgehog pathway modulation by multiple lipid binding sites on the smoothened effector of signal response. Dev. Cell 26, 346–357.

Myers, B.R., Neahring, L., Zhang, Y., Roberts, K.J., and Beachy, P.A. (2017). Rapid, direct activity assays for Smoothened reveal Hedgehog pathway regulation by membrane cholesterol and extracellular sodium. Proc. Natl. Acad. Sci. USA 114, E11141–E11150.

Nakane, T., Kimanius, D., Lindahl, E., and Scheres, S.H. (2018). Characterisation of molecular motions in cryo-EM single-particle data by multi-body refinement in RELION. eLife 7, e36861.

Pepinsky, R.B., Zeng, C., Wen, D., Rayhorn, P., Baker, D.P., Williams, K.P., Bixler, S.A., Ambrose, C.M., Garber, E.A., Miatkowski, K., et al. (1998). Identification of a palmitic acid-modified form of human Sonic hedgehog. J. Biol. Chem. 273, 14037–14045.

Pettersen, E.F., Goddard, T.D., Huang, C.C., Couch, G.S., Greenblatt, D.M., Meng, E.C., and Ferrin, T.E. (2004). UCSF Chimera–a visualization system for exploratory research and analysis. J. Comput. Chem. 25, 1605–1612.

Punjani, A., Rubinstein, J.L., Fleet, D.J., and Brubaker, M.A. (2017). cryoSPARC: algorithms for rapid unsupervised cryo-EM structure determination. Nat. Methods 14, 290–296.

Qi, X., Schmiege, P., Coutavas, E., and Li, X. (2018a). Two Patched molecules engage distinct sites on Hedgehog yielding a signaling-competent complex. Science 362, eaas8843.

Qi, X., Schmiege, P., Coutavas, E., Wang, J., and Li, X. (2018b). Structures of human Patched and its complex with native palmitoylated sonic hedgehog. Nature 560, 128–132.

Raleigh, D.R., Sever, N., Choksi, P.K., Sigg, M.A., Hines, K.M., Thompson, B.M., Elnatan, D., Jaishankar, P., Bisignano, P., Garcia-Gonzalo, F.R., et al. (2018). Cilia-Associated Oxysterols Activate Smoothened. Mol. Cell 72, 1–12.

Rhim, A.D., Oberstein, P.E., Thomas, D.H., Mirek, E.T., Palermo, C.F., Sastra, S.A., Dekleva, E.N., Saunders, T., Becerra, C.P., Tattersall, I.W., et al. (2014). Stromal elements act to restrain, rather than support, pancreatic ductal adenocarcinoma. Cancer Cell 25, 735–747.

Roessler, E., Belloni, E., Gaudenz, K., Jay, P., Berta, P., Scherer, S.W., Tsui, L.C., and Muenke, M. (1996). Mutations in the human Sonic Hedgehog gene cause holoprosencephaly. Nat. Genet. 14, 357–360.

Rogers, H.W., Weinstock, M.A., Feldman, S.R., and Coldiron, B.M. (2015). Incidence Estimate of Nonmelanoma Skin Cancer (Keratinocyte Carcinomas) in the U.S. Population, 2012. JAMA Dermatol. 151, 1081–1086.

Rohatgi, R., Milenkovic, L., and Scott, M.P. (2007). Patched1 regulates hedgehog signaling at the primary cilium. Science 317, 372–376.

Scheres, S.H. (2012). RELION: implementation of a Bayesian approach to cryo-EM structure determination. J Struct. Biol. 180, 519–530.

Shin, K., Lee, J., Guo, N., Kim, J., Lim, A., Qu, L., Mysorekar, I.U., and Beachy, P.A. (2011). Hedgehog/Wnt feedback supports regenerative proliferation of epithelial stem cells in bladder. Nature 472, 110–114.

Shin, K., Lim, A., Zhao, C., Sahoo, D., Pan, Y., Spiekerkoetter, E., Liao, J.C., and Beachy, P.A. (2014). Hedgehog signaling restrains bladder cancer progression by eliciting stromal production of urothelial differentiation factors. Cancer Cell 26, 521–533.

Stone, D.M., Hynes, M., Armanini, M., Swanson, T.A., Gu, Q., Johnson, R.L., Scott, M.P., Pennica, D., Goddard, A., Phillips, H., et al. (1996). The tumoursuppressor gene patched encodes a candidate receptor for Sonic hedgehog. Nature 384, 129–134.

Taipale, J., Cooper, M.K., Maiti, T., and Beachy, P.A. (2002). Patched acts catalytically to suppress the activity of Smoothened. Nature 418, 892–897.

Tamura, N., Murakami, S., Oyama, Y., Ishiguro, M., and Yamaguchi, A. (2005). Direct interaction of multidrug efflux transporter AcrB and outer membrane channel TolC detected via site-directed disulfide cross-linking. Biochemistry 44, 11115–11121.

Teglund, S., and Toftgård, R. (2010). Hedgehog beyond medulloblastoma and basal cell carcinoma. Biochim. Biophys. Acta 1805, 181–208.

Tsukazaki, T., and Nureki, O. (2011). The mechanism of protein export enhancement by the SecDF membrane component. Biophysics (Nagoyashi) 7, 129–133.

Wang, H., Shi, Y., Song, J., Qi, J., Lu, G., Yan, J., and Gao, G.F. (2016). Ebola Viral Glycoprotein Bound to Its Endosomal Receptor Niemann-Pick C1. Cell 164, 258–268.

Xiao, X., Tang, J.J., Peng, C., Wang, Y., Fu, L., Qiu, Z.P., Xiong, Y., Yang, L.F., Cui, H.W., He, X.L., et al. (2017). Cholesterol Modification of Smoothened Is Required for Hedgehog Signaling. Mol. Cell 66, 154–162.e10.

Yoon, Y., Lee, P.J., Kurilova, S., and Cho, W. (2011). In situ quantitative imaging of cellular lipids using molecular sensors. Nat. Chem. 3, 868–874.

Zhang, K. (2016). Gctf: Real-time CTF determination and correction. J. Struct. Biol. 193, 1–12.

Zheng, S.Q., Palovcak, E., Armache, J.P., Verba, K.A., Cheng, Y., and Agard, D.A. (2017). MotionCor2: anisotropic correction of beam-induced motion for improved cryo-electron microscopy. Nat. Methods 14, 331–332.

Zheng, X., Mann, R.K., Sever, N., and Beachy, P.A. (2010). Genetic and biochemical definition of the Hedgehog receptor. Genes Dev. 24, 57–71.

# STAR★METHODS

## KEY RESOURCES TABLE

| REAGENT or RESOURCE | SOURCE | IDENTIFIER |
|---|---|---|
| **Antibodies** | | |
| HA Tag Monoclonal Antibody (2-2.2.14), HRP | ThermoFisher | 26183-HRP; RRID: AB_2533056 |
| [K(Ac)40]α-Tubulin polyclonal antibody | Enzo | BML-SA452; RRID: AB_10554725 |
| Alexa Fluor 568 Goat Anti-Rabbit IgG (H+L) *Highly Cross-Adsorbed* | ThermoFisher | A-11036; RRID: AB_143011 |
| Streptavidin, AlexaFluor 647 conjugate | ThermoFisher | S-32357 |
| **Bacterial and Virus Strains** | | |
| BL21(DE3) Competent *E. coli* | NEB | C2527H |
| BL21-CodonPlus(DE3) -RIL Competent Cells | Agilent | 230245 |
| GCI-5α Chemically Competent E.coli Cells, | GeneCopoeia | CC002 |
| **Chemicals, Peptides, and Recombinant Proteins** | | |
| n-Dodecyl-B-D-maltopyranoside | Anatrace | D310 5 GM |
| Cholesteryl Hemisuccinate Tris Salt | Anatrace | CH210 5 GM |
| Iodoacetamide SigmaUltra | Sigma | I1149-5G |
| D-Biotin, Fisher BioReagents | Fisher | BP232-1 |
| Acrylodan | ThermoFisher | A433 |
| (2Z,3E)-3-((acryloyloxy)imino)-2-((7-(diethylamino)-9, 9-dimethyl-9H-fluoren-2-yl)methylene)-2,3-dihydro-1H-inden-1-one (WCR) | This paper | N/A |
| Sucrose octasulfate (potassium salt) | Cayman Chemicals | 16382 |
| Sf-900 II SFM medium | ThermoFisher | 10902-088 |
| Freestyle 293 medium | ThermoFisher | 12338-018 |
| Cellfectin II reagent | ThermoFisher | 10362-100 |
| BestBac 1.0, Linearized Baculovirus DNA | ExpressionSystems | 91-001 |
| Pierce Protease Inhibitor Tablets | ThermoFisher | PIA32965 |
| EZ-Link Maleimide PEG2-Biotin | ThermoFisher | 21901BID |
| **Critical Commercial Assays** | | |
| High capacity streptavidin resin | ThermoFisher | 20361 |
| Superdex 200, 10/300 GL | GE Healthcare | 17517501 |
| HiTrap SP FF column | GE Healthcare | 17505401 |
| SEC-5 HPLC column | Agilent | 5190-2528 |
| HPLC column | Wyatt | WTC-030S5 |
| Dual-luciferase reporter assay | Promega | E1960 |
| SulfoLink Coupling Resin | ThermoFisher | 20401 |
| **Deposited Data** | | |
| Structure of mouse Ptch1 | This paper | PDB: 6MG8 |
| Cryo-EM maps of mouse Ptch1 | This paper | EMDB: EMD-9111 |
| **Experimental Models: Cell Lines** | | |
| P2A6 Ptch1⁻/⁻ fibroblast | Taipale et al., 2002 | N/A |
| Freestyle 293 cells | ThermoFisher | R79007 |
| Sf9 cells | ATCC | CRL-1711 |
| 293FT cells | ThermoFisher | R70007 |
| **Software and Algorithms** | | |
| Astra | Wyatt | https://www.wyatt.com/ |
| Relion2.0 | Scheres, 2012 | https://www2.mrc-lmb.cam.ac.uk/relion |

*(Continued on next page)*

***Continued***

| REAGENT or RESOURCE | SOURCE | IDENTIFIER |
|---|---|---|
| Cryosparc | Punjani et al.,2017 | https://cryosparc.com/ |
| Gctf | Zhang, 2016 | N/A |
| Gautomatch | Zhang, 2016 | N/A |
| MotionCorr2 | Zheng et al., 2017 | N/A |
| COOT | Emsley et al., 2010 | https://www2.mrc-lmb.cam.ac.uk/Personal/pemsley/coot/ |
| Phenix | Afonine et al., 2012 | https://www.phenix-online.org/ |
| PyMOL | Schrödinger | https://pymol.org/2/ |
| UCSF Chimera | Pettersen et al., 2004 | https://www.cgl.ucsf.edu/chimera/ |
| UCSF ChimeraX | Goddard et al., 2018 | https://www.rbvi.ucsf.edu/chimerax/ |
| Pyem | Github | https://github.com/asarnow/pyem |
| Oligonucleotides | | |
| gBlock for SBP tag: ATGGATGAAAAGACCACCGGTTGGCGTGGTGGTCATGTTGTTGAAGGTCTGGCAGGCGAACTGGAACAGCTGCGTGCACGTCTGGAACATCATCCGCAGGGTCAGCGTGAACCG | IDT | N/A |
| Primers for cloning | See Table S1 | N/A |
| Recombinant DNA | | |
| pVLAD6-mmPtch1-B-SBP | This paper | N/A |
| pcDNA-h-mmPtch1-B | This paper | N/A |
| pcDNA-h-mmPtch1-FL | This paper | N/A |
| pcDNA-h-mmPtch1-B-HA | This paper | N/A |
| pcDNA-h-mmPtch1-B-Y233C-HA | This paper | N/A |
| pcDNA-h-mmPtch1-B-L234C-HA | This paper | N/A |
| pcDNA-h-mmPtch1-B-L235C-HA | This paper | N/A |
| pcDNA-h-mmPtch1-B-HA-GFP | This paper | N/A |
| pcDNA-h-mmPtch1-B-NNQ-HA-GFP | This paper | N/A |
| pcDNA-h-mmPtch1-B-I766FV111F-HA-GFP | This paper | N/A |
| pcDNA-h-mmPtch1-B-V111FL114FW115A-HA-GFP | This paper | N/A |
| pcDNA-h-mmPtch1-B-I766FV111FL114F-HA-GFP | This paper | N/A |
| pcDNA-h-mmPtch1-B-HA-TagBFP | This paper | N/A |
| pcDNA-h-mmPtch1-FL-TagBFP | This paper | N/A |
| pcDNA-h-mmPtch1-B-NNQ-HA | This paper | N/A |
| pcDNA-h-mmPtch1-B-V111FL114FI766F-HA | This paper | N/A |
| pcDNA-h-mmPtch1-B-V111FL114FI766F-HA-TagBFP | This paper | N/A |
| pHTSHP-ShhN-GFP | This paper | N/A |
| pHTSHP-ShhN-Cys | This paper | N/A |
| pHTSHP-Smt-IIShhN | This paper | N/A |
| pLAP1-NPHP2 | Gift from Peter Jackson's lab, Stanford | N/A |
| SV40-Renilla Luciferase | Kim et al., 2009 | N/A |
| 8xGli Firefly Luciferase | Kim et al., 2009 | N/A |

## CONTACT FOR REAGENT AND RESOURCE SHARING

Further information and requests for resources and reagents should be directed to and will be fulfilled by the Lead Contact, Philip A. Beachy (pbeachy@stanford.edu).

## EXPERIMENTAL MODEL AND SUBJECT DETAILS

Sf9 and 293T cells were maintained in culture according to previously published conditions (Myers et al., 2013). Sf9 cells were grown in Sf-900 III medium supplemented with 10% fetal bovine serum (FBS, Gemini Bio). 293T cells were cultured in DMEM medium supplemented with 10% FBS and glutamine. 293-Freestyle cells were maintained in suspension culture in an 8% $CO_2$ incubator equipped with a shaking platform, using Freestyle 293 expression medium (ThermoFisher) supplemented with 1% FBS. $Ptch1^{-/-}$ MEFs were maintained as previously described (Myers et al., 2017) in DMEM medium supplemented with 10% FBS and glutamine. No special efforts were done to authenticate the cell lines.

## METHOD DETAILS

### Molecular cloning

All constructs were cloned with Gibson assembly. For BacMam expression, PTCH1 variants were cloned into pVLAD6 vector. Ptch1-A contains 1-1291 of the amino acid sequence of mouse (*Mus musculus*) PTCH1 isoform a. Ptch1-B contains an additional deletion of amino acids 620-643 from Ptch1-A. For luciferase assay and cell surface binding experiments, PTCH1 variants were cloned into pcDNA-h vector, a vector derived from pcDNA3 with the neomycin resistance cassette removed (created by Huai-hu Chuang, Academia Sinica, Taipei, Taiwan. The fragment removed corresponds to nucleotides 1308-3243 in the pcDNA3.1+ sequence from ThermoFisher). Primers for cloning were listed in Table S1.

### PTCH1 purification

Baculovirus production in Sf9 cells and infection of suspension 293 cultures with recombinant baculovirus (BacMam expression) was performed as previously described (Myers et al., 2013). In brief, pVLAD6 plasmid along with the linearized baculovirus DNA (BestBac, Expression Systems) was transfected into Sf9 cells using Cellfectin II, following vendor's instructions. Virus harvested 5-7 days in the supernatant was then amplified in Sf9 cells. Suspension 293 cells were grown to a density of $1.2 – 1.6 \times 10^6$/ml, supplemented with 10 mM sodium butyrate, and infected with 3% (v/v) high-titer Ptch1-SBP baculoviruses as determined by titration for 40-48 hr. Cell pellets were stored at $-80°C$. Pellets were thawed into hypotonic buffer (20 mM HEPES pH 7.5, 10 mM $MgCl_2$, 10 mM KCl, 0.25 M sucrose) supplemented with protease inhibitors and benzonase. Crude membranes were pelleted with centrifugation (100,000 x g, 30 min., 4°C). The pellet was resuspended in lysis buffer (300 mM NaCl, 20 mM HEPES pH 7.5, 2mg/ml iodoacetamide, 1% DDM / 0.2% CHS) with protease inhibitors and solubilized for 1 hour at 4°C with gentle rotation. After centrifugation (100,000 x g, 30 min., 4°C), the supernatant was incubated with streptavidin-agarose affinity resin in batch mode for 2-3 hours at 4°C with gentle rotation. The resin was packed into a disposable column, and washed with 20-30 column volumes of buffer (20 mM HEPES pH 7.5, 300 mM NaCl, 0.03% DDM / 0.006% CHS). Protein was eluted in the same buffer supplemented with 2.5 mM biotin. Purified Ptch1-B protein was then mixed with PMAL-C8 at 1:3 mass ratio and dialyzed against detergent free buffer (20 mM HEPES, pH 7.5, 300 mM NaCl, 0.5 mM $CaCl_2$) overnight in a dialysis cassette with molecular weight cutoff of 100 kDa.

### Multiangle light scattering

Purified Ptch1-B was exchanged into Amphipol A8-35 in the same way as the exchange into PMAL-C8. The protein was then loaded onto an HPLC column for SEC-MALS (Wyatt Technology). UV extinction coefficient for Ptch1-B was calculated with the ProtParam program on the ExPasy server (https://expasy.org) to be 1.280 mL /(g cm). The dn/dc values were according to previous reports (Constantine et al., 2016), namely, 0.185 mL/g for proteins, 0.1424 mL/g for A8-35. The UV extinction coefficient for A8-35 is 0.0386 (Constantine et al., 2016). Data were analyzed with Astra6 software.

### Purification of Shh variants

The cysteine variant of Shh (ShhNCys) was obtained by cloning the DNA fragment encoding mouse Sonic hedgehog residues 26-190 (ShhN) followed by a Cysteine into pHTSHP vector (described in (McLellan et al., 2008)). Isoleucine variant of Shh (IIShhN) was obtained by cloning SUMO tag, two isoleucines, then mouse Shh 26-190 into pHTSHP vector. Proteins were expressed in *E. coli* strain BL21(DE3) and purified according to the protocol described in ref. (Cleveland et al., 2014), with minor modifications. In brief, for the cysteine variant, 2 mM TCEP was included in all the buffers used during purification, to keep the cysteine reduced. After purification by immobilized metal ion chromatography (IMAC), the N-terminal tags for the cysteine variant were cleaved with HRV3C protease, whereas for IIShhN tags were cleaved with SUMO protease. The protein was dialyzed against 20 mM HEPES, 150 mM NaCl and 7 mM β-ME overnight at 4°C and further purified by cation-exchange chromatography.

### Biotinylation of purified ShhN protein

After elution from a Ni-NTA column, ShhNCys protein was mixed with EZ-link maleimide-biotin (ThermoFisher) at 1:10 molar ratio and reacted at room temperature for 1 hr. The reaction mixture was then diluted 10-fold with Ni loading buffer (300 mM NaCl, 20 mM HEPES, pH 7.5) and loaded onto a Ni-NTA column. After elution with imidazole, the protein was dialyzed and further purified with cation exchange chromatography as in the section above.

### Preparation of Shh affinity resin

Purified ShhNCys was then diluted into resin coupling buffer (50 mM Bicine pH 8, 800 mM NaCl, 5 mM EDTA) and then incubated with pre-equilibrated SulfoLink Coupling Resin (ThermoFisher) overnight at 4 °C. Coupling reaction was monitored by UV absorbance at 280 nm. After coupling, the resin was washed twice with the coupling buffer, and then blocked with 10 mM sodium 2-mercaptoethanesulfonate (MESNA) in the coupling buffer. The resin was then washed with 20 mM HEPES, 300 mM NaCl, 10 μM $ZnSO_4$, to restore zinc chelation on ShhN, and stored in the same buffer with azide.

### Shh affinity purification

Shh affinity resin was packed into a disposable column. After equilibration with detergent free buffer (20 mM HEPES, 300 mM NaCl, 0.5 mM $CaCl_2$), the column was loaded with purified PTCH1. After the protein passed through, the resin was washed with the same buffer. PTCH1 was eluted with ∼2 μM purified IIShhN. The eluted protein was concentrated with an Amicon filter with a 100 kDa cutoff, and then loaded onto Superdex 200 column. Peak fractions were collected for later structure resolution.

### Cryo-EM sample preparation

Purified Ptch1-B:IIShhN complex was concentrated with an Amicon filter (100 kDa cutoff) to a concentration of ∼0.6 mg/ml. Sucrose octasulfate (SOS, Santa Cruz) was then added to a concentration of 2.5 mM and incubated overnight. 2.5 μL sample was applied to a glow-discharged quantifoil grid on a vitrobot. The sample chamber was kept at 100% relative humidity. The grid was blotted for 5 s and plunged into liquid ethane bath cooled by liquid nitrogen.

### Cryo-EM Data aquisition

The cryo grids were imaged on the Janelia Krios 2, an FEI Titan Krios EM operated at 300 kV. Images were taken on the pre-GIF K2 camera in dose fractionation mode, at nominal magnification of 22.5k, corresponding to a pixel size of 1.31 Å (0.655 Å per super-resolution pixel). The total exposure time was 8 s, with 0.2 s per frame. Fully automated data collection was performed with SerialEM, with a defocus range of −1 μm to −3 μm. Gain reference was taken at the beginning of the data collection and was applied later in data processing.

### Image processing

A total of 5236 movie stacks were collected. The movie stacks were corrected by gain reference, binned by 2, and corrected for beam-induced motion with MotionCor2. CTF was determined with GCTF from the motion-corrected sums without dose-weighting. Dose-weighted sums were used for all the following steps of processing. Particles were autopicked with Gautomatch. The following processing was all done in cryo-SPARC. Particles corresponding to protein molecules were selected from 2D classification. These particles were then reconstructed *ab initio*, and then classified with heterogeneous refinement into 3 classes, using the map generated from the last step plus two junk maps as the initial models. The best class was chosen for homogeneous refinement and then homogeneous refinement++ to obtain the final 3.7 Å map. The same set of particles was then refined with imposition of C2 symmetry to obtain a symmetrized 3.5 Å map.

### Multi-body Refinement

In order to investigate the nature of the weakly resolved subunit, and to better classify conformational heterogeneity in both subunits, we extended our single-particle reconstruction with multi-body analysis. In this approach, partial signal subtraction(Bai et al., 2015) and local pose transformations(Ilca et al., 2015) are used to refine the two subunits first as independent rigid bodies, and subsequently as a single, combined body. The differential resolution of the two subunits presents a difficulty, in that accurate signal subtraction depends in turn on accurate estimates of particle pose. We thus carried out multi-body refinements in serial, first refining the weak subunit and then using the new density and pose estimates for subtraction during refinement of the strong subunit.

Briefly, a target point was identified near the protein center-of-mass, ignoring amphipol density, in the weak subunit. All masks, references, and reconstruction parameters (particle metadata) were transformed to center this target point in the reconstruction volume. CTF-filtered projections of the density corresponding to the strong subunit were subtracted from particle images using single-body reconstruction parameters. The subtracted images were subjected to 3D refinement in Relion with local angular and translational searches, yielding a greatly improved structure of the weak subunit. With density for the weak subunit of sufficient quality for signal subtraction now in hand, we repeated the procedure using the conjugate target point for the strong subunit. Finally, reference maps and reconstruction parameters for the two independent bodies were transformed so as to precisely overlay, and a final combined refinement was performed. The combined refinement yielded the highest quality density map of a Ptch1-B monomer, presumably due to the two-fold increase in effective particle count as well as the greatly simplified alignment problem. Improvements over previous results were critical in completing our atomic model of Ptch1-B, and in identifying the extra lipid-like densities. Classification after single-subunit and combined monomer refinement was also critical in rejecting putative alternate conformations identified during conventional single-particle analysis due to pervasive misalignment of the subunits.

In addition to improved reconstructions, the multi-body approach enables global analysis of *residual pose transformations*. These residuals are defined as the deltas between the initial pose of each particle from conventional SPA, and the final pose obtained after independent body refinement (i.e., based on inverse rotations and negative shifts). In order to better understand relative subunit

displacements in Ptch1-B dimers, we computed residual rotations and subjected these to kernel principal component analysis under a kernel derived from the geodesic on the manifold of 3D rotations. Use of the geodesic kernel is important due to the intrinsic curvature of the manifold. While the manifold may be locally linear in the context of small residuals, in our hands the mean and standard deviation magnitudes were 9.2° and 3.4°, respectively, implying that error due to curvature would be ~10% at one standard deviation from the mean. Further, while results from local pose searches are presented here, we found that global searches were successful for Ptch1-B subunits and also permit residual pose calculations modulo alignment of the references.

All multi-body analysis in this work was performed using UCSF PyEM (for local transformations and orientation analysis) in concert with Relion (for 3D classification and refinement). During the preparation of this manuscript, a paper described a method for automated multi-body refinement that has been integrated into Relion (Nakane et al., 2018). The described method is similar to ours, but was not available for comparison at the time of submission. UCSF PyEM is provided under the GNU Public License, version 3, and may be accessed at https://github.com/asarnow/pyem.

### Structure modeling
The atomic model of PTCH1 was manually built in COOT (Emsley et al., 2010), using both the dimer and the monomer maps from cryo-EM. The model was then refined with Phenix real space refinement (Afonine et al., 2012). Figures of the structures were prepared with PyMOL, UCSF Chimera and UCSF ChimeraX.

### *In vitro* ShhN binding assay
Purified Ptch1 protein in PMAL-C8 was further purified with gel filtration in 20 mM HEPES, 300 mM NaCl and 0.5 mM $CaCl_2$. The peak fractions were collected and concentrated with a 100 kDa cutoff Amicon ultrafiltration device. Serial dilutions of the purified Ptch1 protein were added to gel-filtration buffer supplemented with 0.1 mg/ml BSA. GFP-tagged ShhN was diluted with the same buffer to 40 nM and mixed at 1:1 volume with diluted Ptch1 protein. Interaction was measured via microscale thermophoresis and data were processed with Nanotemper NTA Affinities.

### FACS-based ShhN binding assay
293 cells were transiently transfected with GFP-tagged Ptch1 constructs. After 24 hours, cells were dissociated using 10 mM EDTA, washed with HPBS 0.5 mM $Ca^{2+}$, and pelleted by centrifugation. Cells were then resuspended in binding buffer (HPBS, 0.5 mM $Ca^{2+}$, 0.5 mg/ml BSA) and incubated with purified ShhN-biotin (1:400 dilution) for 30 minutes at 4°C. Cells were then washed three times in binding buffer by centrifugation and subsequently incubated with Alexa Fluor 647 streptavidin conjugate (Invitrogen) for 15 minutes at 4°C. Cells were then washed three times by centrifugation in wash buffer (binding buffer plus 1 mM biotin) and the percentages of cells bound by ShhN were quantified by flow cytometry after gating for PTCH1-GFP expression (BD FACSAria II, Stanford Stem Cell Institute FACS Core).

### Gli-dependent luciferase assay
The luciferase assay was performed in Ptch1$^{-/-}$ MEFs, as previously described(Myers et al., 2017). Ptch1$^{-/-}$ MEFs were seeded into 24-well plates and then transfected with various plasmids along with a mixture containing 8xGli firefly luciferase and SV40-renilla luciferase plasmids. For each well, 2ng (0.4%) plasmid encoding Ptch1-B variants, or 5ng (1%) plasmid encoding full-length PTCH1 was used. When cells were confluent, they were shifted to DMEM with 0.5% serum containing ShhN-conditioned medium or control medium and incubated for 48 hr. Luciferase activity was then measured using a Berthold Centro XS3 luminometer. The ShhN conditioned medium was prepared from 293 cells transfected with a plasmid expressing the amino signaling domain of Shh. In brief, 293 cells were transfected with the ShhN expression plasmid with lipofectamine 2000. Twelve hours after transfection, culture medium was replaced with 2% FBS low-serum medium. The conditioned medium was then collected 48hours after medium change, and used at 1:10 for the luciferase assays.

### Cellular cholesterol measurement
The PFO D4 domain (aa 391–500) and mutants were expressed as His$_6$–tagged proteins in *E. coli* BL21 RIL codon plus (Stratagene) cells and purified using the His$_6$–affinity resin (GenScript). These proteins were labeled at the single Cys site (C459) by a solvatochromic fluorophore to generate ratiometric sensors.

HEK293 cells or Ptch1$^{-/-}$ MEFs were seeded into 50 mm round glass–bottom plates (MatTek) and grown at 37°C in a humidified atmosphere of 95% air and 5% $CO_2$ in Dulbecco's modified Eagle's medium (DMEM) (Life Technologies) supplemented with 10% (v/v) fatal bovine serum (FBS), 100 U/ml penicillin G, and 100 μg/ml streptomycin sulfate (Life Technologies).

After attachment to the culture vessels (~24hr), cells were transiently transfected with plasmids encoding Ptch1-B variants using the jetPRIME transfection reagent (Polyplus Transfection) according to the manufacturer's protocol. 1 μg plasmid was used for each transfection to achieve a concentration of 1 μg/ml in the transfection mix. For titration of Ptch1 expression levels, varying amounts of Ptch1 plasmid were mixed with 8xGli firefly luciferase plasmid to add up to 1 μg/ml of total DNA in the transfection mix. Ten hours after transfection, cholesterol in the inner (IPM) and the outer (OPM) leaflets of the plasma membrane was quantified simultaneously using orthogonal cholesterol sensors as described previously (Liu et al., 2017) with some modification. Specifically, the wild-type D4 domain labeled with acrylodan (DAN) (ThermoFisher) was added to the cells for quantification of OPM cholesterol ([Chol]$_o$)

whereas the Y415A/D434W/A463W (YDA) mutant of the D4 domain labeled with (2Z,3E)-3-((acryloyloxy)imino)-2-((7-(diethylamino)-9,9-dimethyl-9H-fluoren-2-yl)methylene)-2,3-dihydro-1H-inden-1-one (WCRX) was delivered into the cells by microinjection for quantification of IPM cholesterol ($[Chol]_i$). WCRX was prepared from 2,7-dibromo-9,9-dimethyl-9H-fluorene (Sigma-Aldrich) by a four-step synthesis (30% overall yield) and confirmed by NMR spectroscopy and mass spectrometry. Detailed synthesis and spectral characterization of WCRX will be published elsewhere. All sensor calibration, microscopy measurements, and ratiometric imaging data analysis were performed as described (Liu et al., 2017; Liu et al., 2014; Yoon et al., 2011). In brief, YDA-WCRX and D4-DAN were calibrated using giant unilamellar vesicles whose lipid compositions recapitulate those of IPM (i.e., 1-palmitoyl-2-oleoyl-sn-glycero-3-phosphocholine (POPC)/1-palmitoyl-2-oleoyl-sn-glycero-3-phosphoethanolamine (POPE)/ 1-palmitoyl-2-oleoyl-sn-glycero-3-phosphoserine (POPS)/ liver phosphatidylinositol (PI)/cholesterol/ 1,2-dipalitoyl-phosphatidylinositol-4,5-bisphosphate (PI45P$_2$) (20/50-x/20/9/x/1: $x$ = 0-20 mole%) and OPM (i.e., POPC/ porcine brain sphingomyelin (SM)/cholesterol (70-x/30/x: $x$ = 0-60 mole%), respectively, with a custom-modified six-channel FV3000 (Olympus) confocal laser scanning microscope. D4-DAN and YDA-WCRX were excited by 405-nm and 488-nm laser sources, respectively. Fluorescence emission of D4-DAN was measured in two separate channels with the spectral detector setting of 460-480 nm and 515-535 nm, respectively, for ratiometric determination. For YDA-WCRX, two channels with 540-600 nm and 630-660 nm emission setting were employed. Fluorescence intensity ratio values were spatially averaged over the PM for 10-20 different cells at a given time after stimulation and these averaged values were converted into cholesterol concentrations using the calibration curves.

To correlate PTCH1 expression level in transfected cells used for quantification with the expression level that permits Smo regulation in the primary cilia, BFP fluorescence was measured for cells used these two assays. For cells used for cholesterol quantification, mean fluorescence was calculated from the entire cell using Fiji software. To quantify PTCH1 expression in cells used in the luciferase assay, Ptch1−/− MEFs were plated onto a pre-coated 8-well chamber slide. As the area of 8-well chamber roughly corresponds to two 24-well plate wells, cells were transfected with a DNA dose as used for transfection of two wells in the luciferase assay (10 ng Ptch1-B-BFP, 500 ng 8xGli-luciferase, and 100 ng GFP-tagged inversin to mark the primary cilium (kind gift from Peter Jackson, Stanford)). When cells grew to confluency, z stacks were taken for regions with GFP-positive cells on a Zeiss LSM 800 confocal microscrope. The mean BFP intensity was calculated from the ciliary region at the z-level with the best ciliary GFP signal.

To compare endogenous PTCH1 expression level with the expression level used for lipid quantifications, 3T3 cells and Ptch1−/− MEFs were seeded onto MatTek dishes with a No. 1.5 coverslip bottom. Ptch1−/− MEFs were transfected with 100 ng Ptch1-B plasmid along with 900 ng 8xGli firefly luciferase plasmid. Ten hours after transfection, cells were stained with 1 μg/ml biotinylated ShhN diluted in the medium for 10 min, followed by staining with 1:1000 Alexa 647 streptavidin for 10 min. The cells were then fixed with 4% PFA for 5 min. For 3T3 cells, staining was performed similar to the procedure described previously (Rohatgi et al., 2007). Upon reaching confluency, cells were treated with 100 nM SAG for 24hr. The cells were then incubated with 1 μg/ml biotinylated ShhN for 10 min, followed by 1:1000 Alexa 647 streptavidin for 10 min. The cells were then fixed with 4% PFA for 5 min, permeabilized in 0.5% Triton X-100 in PBS for 5 min, blocked in 2 mg/ml BSA in PBS-T (0.1% tween-20) for 15 min, and stained with anti-acetylated tubulin antibody to mark the primary cilium. Incubation with biotinylated ShhN and streptavidin were performed in TC incubator at 37°C. Consistent with previous reports, no specific ShhN staining was seen if cells were fixed with PFA first. Fluorescence was quantified in the Fiji software package. Streptavidin fluorescence in 3T3 cilia was quantified from the ciliary region at the z-level with the best signal of acetylated tubulin. Streptavidin fluorescence of transfected MEFs was quantified around the cell boundary where the signal was strongest.

## QUANTIFICATION AND STATISTICAL ANALYSIS

Data points in figures represent mean values, with error bars in all figures represent standard error of the mean (SEM). Number of replicates is indicated in the figure legends. The sample number n in luciferase assays and FACS-based Shh binding assays represents biological replicates, i.e., independently transfected wells. In cholesterol quantification assays and fluorescence quantification of micrographs, sample number represents the number of cells. No statistical tests were employed to define significance. No statistical methods were used to predetermine sample size.

## DATA AND SOFTWARE AVAILABILITY

The accession number for the PTCH1 structure model reported in this paper is PDB: 6MG8. The accession number for the cryo-EM maps reported in this paper is EMDB: EMD-9111. Further information and requests for scripts used in data processing should be directed to the Lead Contact.
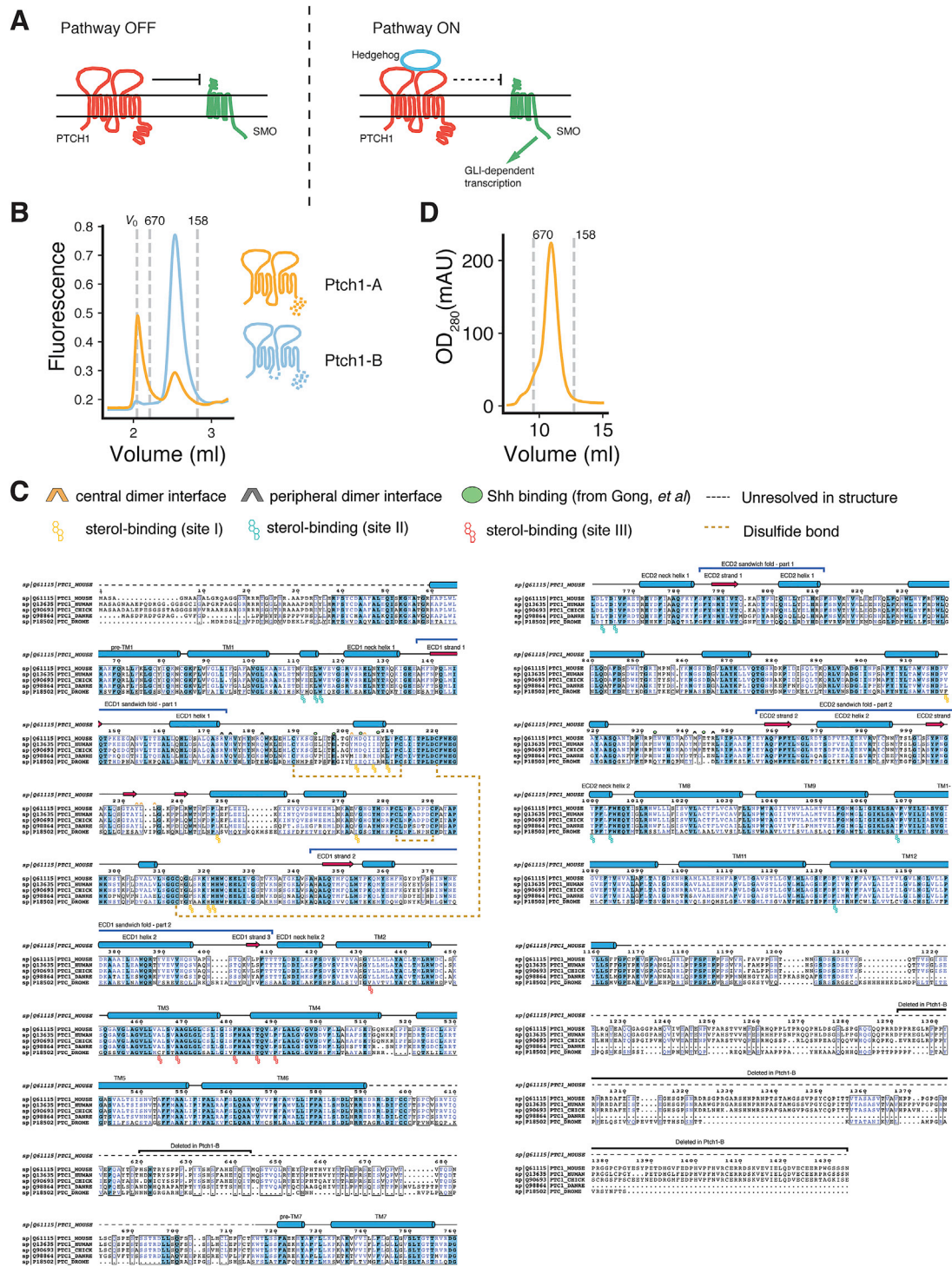
**Figure S1. Patched1 Function and Expression Constructs, Related to Figure 1**

(A) Schematic view of Hedgehog pathway regulation. PTCH1 constitutively suppresses SMO; this suppression is lifted when PTCH1 is bound to Hedgehog, allowing SMO to activate the downstream signaling cascade that activates transcription via GLI transcription factors.

(B) FSEC profile of Ptch1-A and Ptch1-B. Ptch1-A deletes part of the C-terminal sequence, and Ptch1-B in addition deletes some residues in the loop between TM6 and TM7 (see diagrams on the right). Ptch1-B shows a significantly improved FSEC profile. FSEC was done on an Agilent Bio SEC-5 HPLC column.

(C) Sequence alignment of Patched from *Mus musculus* (mouse), *Homo sapiens* (human), *Gallus gallus* (chicken), *Danio rerio* (zebrafish) and *Drosophila melanogaster* (fruit fly), with features from PTCH1 structure marked.

(D) Purified Ptch1-B exhibited a mono-disperse peak in SEC on a Superdex 200 column.
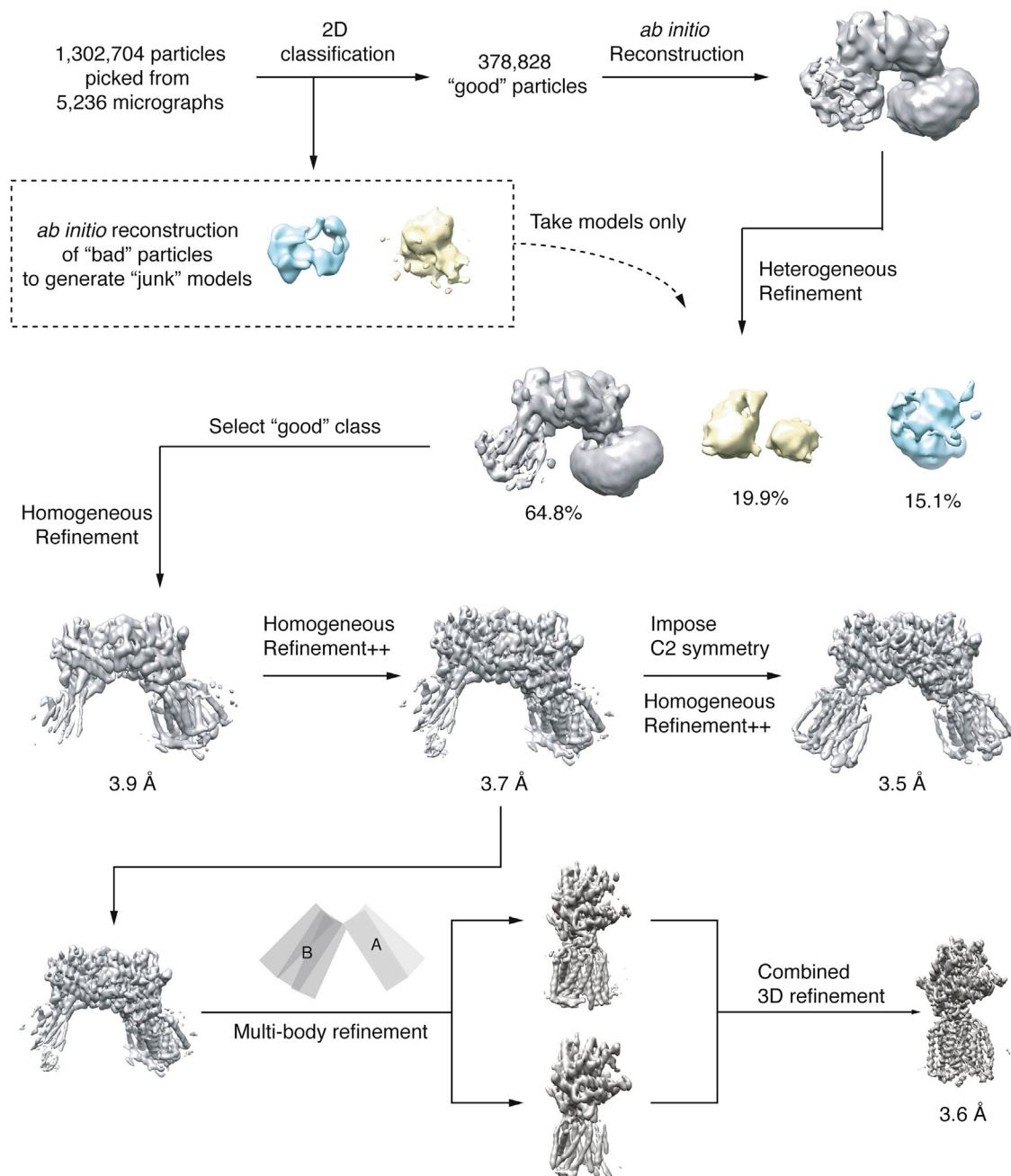
**Figure S2. Data Processing Procedure, Related to Figure 1**

We obtained ~1.3 million particles after auto picking and initiated processing in cryoSPARC. Around 379k particles from 2D classes with clear features were selected to build an initial model with *ab initio* reconstruction; ~400k particles from noisy 2D classes were randomly chosen to generate junk models. The selected protein particles were then classified following the heterogenous refinement protocol, using the initial model plus two junk models as the starting models. About 64% percent of the input particles were retained in the "good" class after this step of classification. We then took the particles and the model from the "good" class for further refinement, first using the "homogenous refinement" and then "homogenous refinement ++" protocol. Finally, we imposed C2 symmetry and repeated "homogenous refinement++" to obtain the symmetrized map. The particles in the non-symmetrized map were subjected to multi-body refinement, assuming a rigid-body like rotation between the two subunits within a dimer. The two subunits were refined independently using the newly determined Euler angles, and then combined in one refinement to generate the high resolution monomer map.
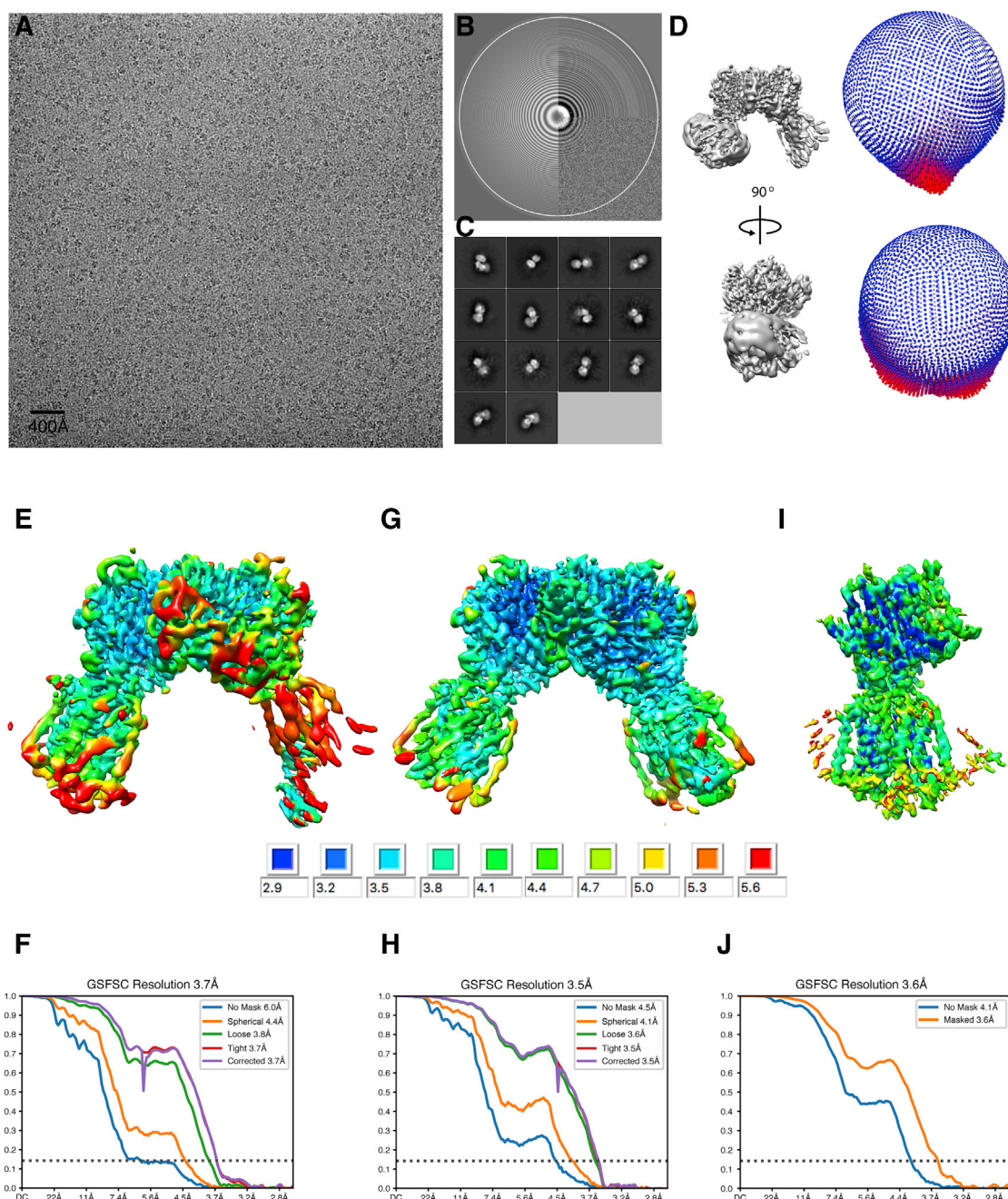
**Figure S3. Overview of Cryo-EM Data, Related to Figure 1 and Table 1**

(A) A representative micrograph of the Ptch1-B sample under cryo-EM, with particles clearly visible.

(B) Parameters of contrast transfer function were determined with GCTF software. Most micrographs have resolution up to 3.0 Å.

(C) 2D class average showing PTCH1 protein dimers.

(D) Euler angle distribution. All orientations are covered in the dataset, but the view from the bottom is somewhat preferred.

(E, G, and I) Local resolution of the electron density map without symmetry (E) or with imposed C2 symmetry (G) revealed that the majority of regions have better than 4 Å resolution. Transmembrane domain in one of the monomers in the non-symmetrized map was poorly resolved. The local resolution shown here was calculated from cryoSPARC. Local resolution of the monomer map from both subunits of the dimer after multi-body refinement is shown in I. Note the improvement in details and local resolution.

(F, H, and J) The global gold-standard Fourier shell correlation (FSC) for the non-symmetrized and the C2 symmetrized maps are shown in panel (F) and (H), respectively. The FSC for the map from multi-body refinement is in panel (J).
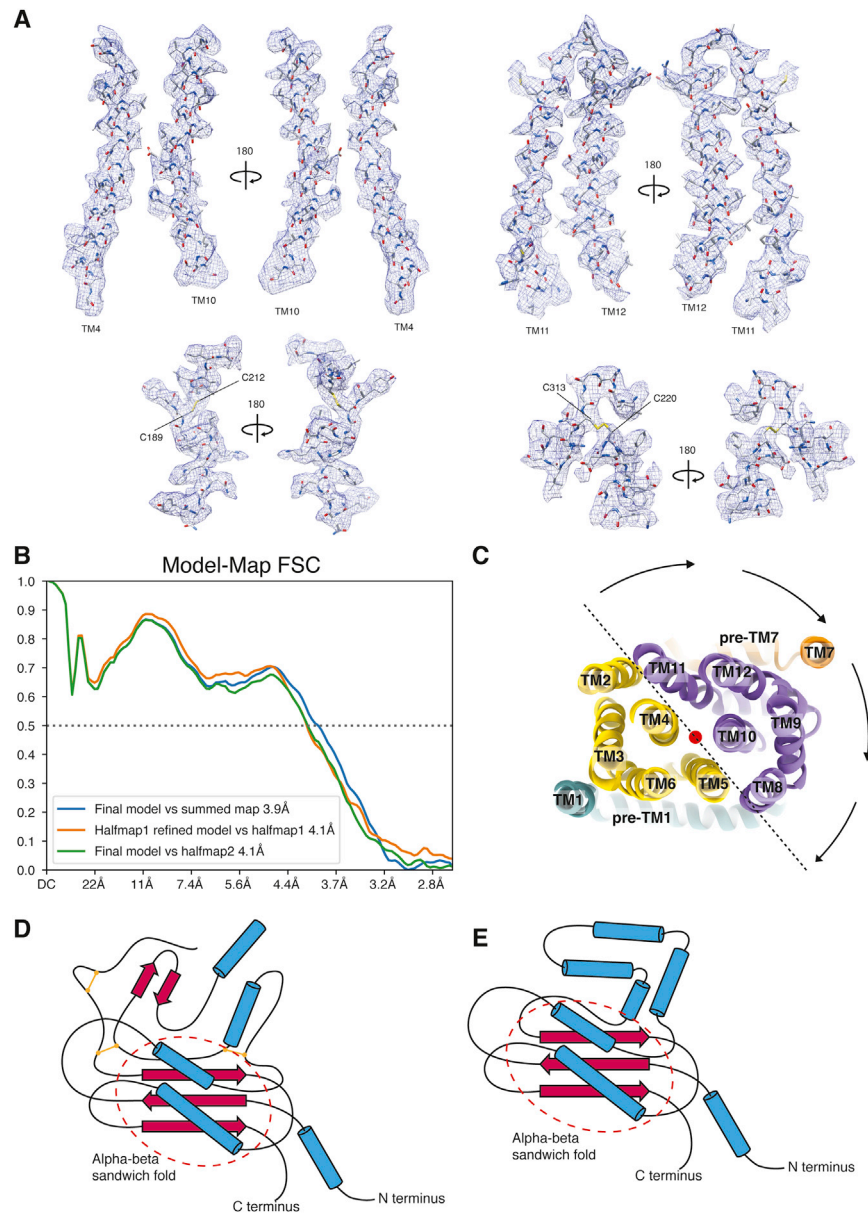
**Figure S4. Features of the Atomic Model as Built into the Density Map, Related to Table 1**

(A) Some regions are selected to show the high quality of the fit between model and density map. Note that the disulfide bond density is visible for two of three disulfides in ECD1.

(B) The FSC between the atomic model of PTCH1 monomer and the maps obtained from refinement of the combined dataset from both subunits. The correlation is above 0.5 up to 3.9 Å resolution.

(C) Section of the PTCH1 transmembrane domain. Pseudo two-fold symmetry centered on the axis indicated by the red dot is evident between TM1-6 and TM7-12.

(D and E) Topology diagram of the extracellular domain between TM1 and TM2 (D), ECD1, and the domain between TM7 and TM8 (E), ECD2.
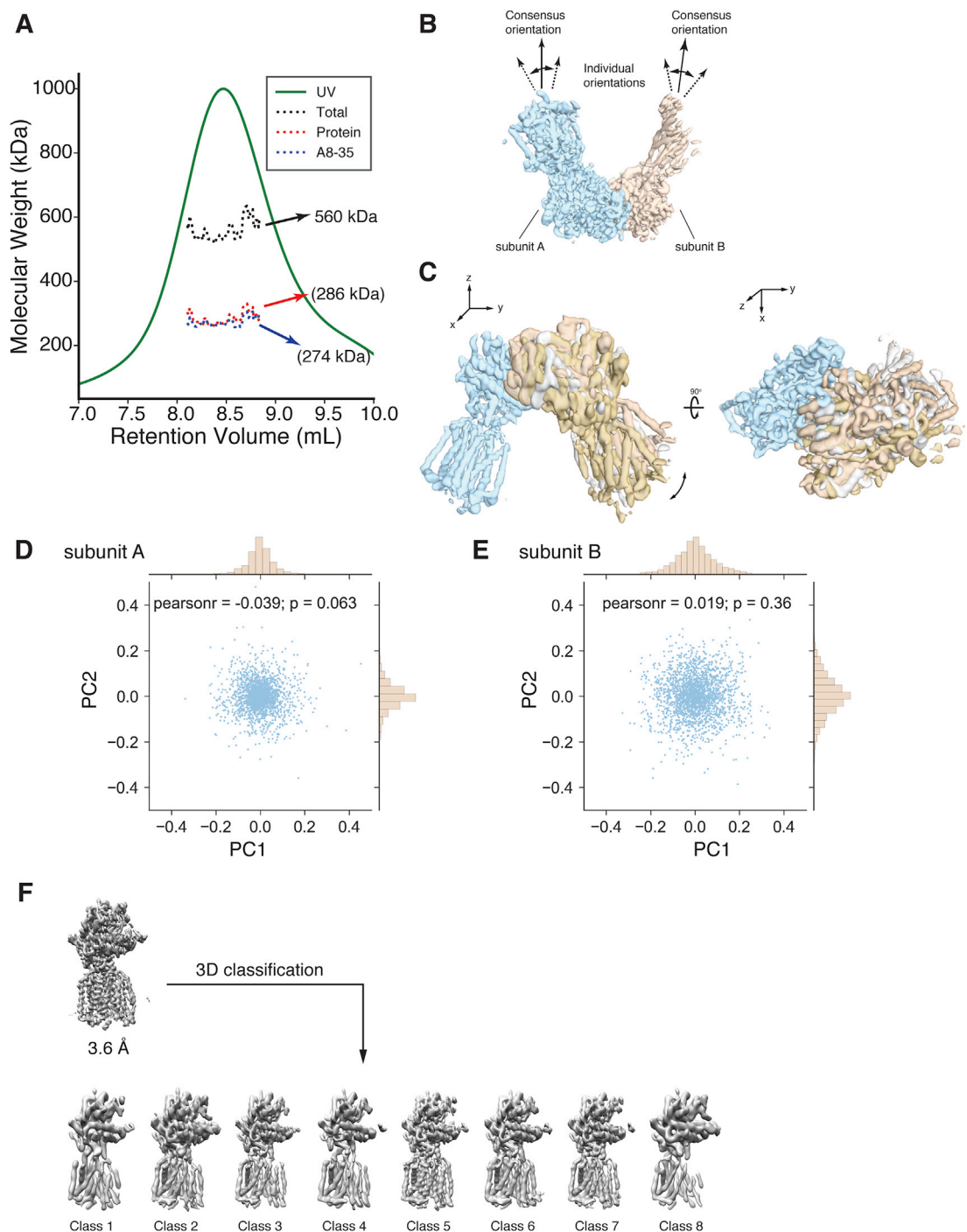
**Figure S5. Characterization of the PTCH1 Dimer, Related to Figure 2**

(A) Molecular weight of the purified protein was determined by SEC-MALS. The protein molecular weight in the SEC peak is ~286 kDa, and the associated detergent micelle (Amphipol A8-35) is ~274 kDa.

(B) The two subunits are treated as rigid body objects to be aligned in the multi-body refinement.

(C) Examples of dimers of distinct relative orientations are superimposed. The blue subunit (left) is aligned as a reference to display relative motion of the other subunit (right). Motions include rotations around both the x and z axes.

(D and E) Euler angle changes were analyzed by kernel principal component analysis (kPCA), using a geodesic kernel on the SO(3) manifold. The first two components for subunit A and B were plotted in (D) and (E) respectively.

(F) The two subunits within a dimer were separated and aligned in the multibody refinement. 3D classification of all monomer subunits combined revealed little difference between the classes. The results suggest that both subunits behave largely as rigid bodies with motion primarily restricted to relative rotation.
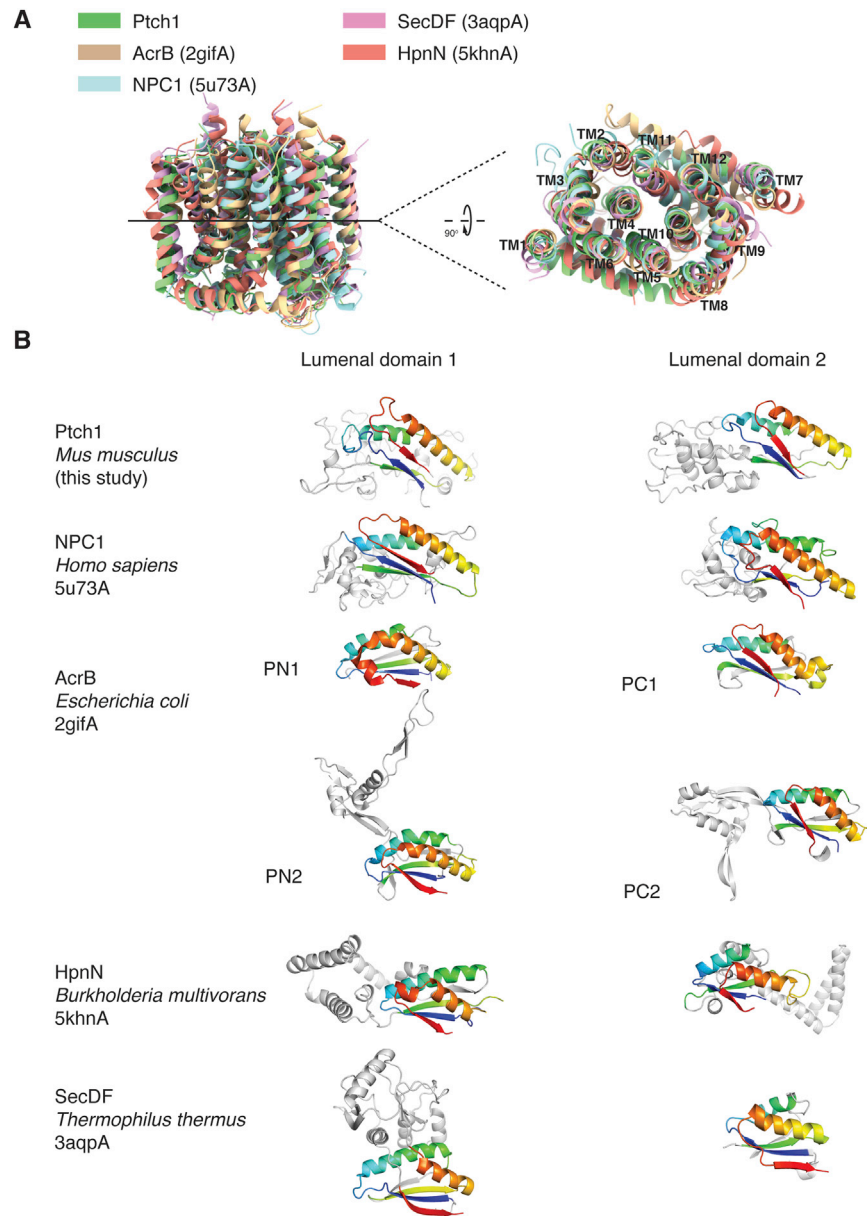
**Figure S6. Comparison of RND Transporters, Related to Figure 3**

(A) Various RND transporters are aligned based on their transmembrane domains. Included are PTCH1 (*Mus musculus*), NPC1 (*Homo sapiens*, 5u73A), AcrB (*Escherichia coli*, 2gifA), HpnN (*Burkholderia multivorans*, 5khnA), and SecDF (*Thermophilus thermus*, 3aqpA).

(B) Shown here is a menu of sandwiches present in the extracellular, periplasmic, or lumenal domains of the proteins mentioned above. In AcrB, two sandwich folds are present within each periplasmic domain, numbered PN1 and PN2 for the TM1-TM2 periplasmic domain and PC1 and PC2 for those in the TM7-TM8 periplasmic domain. Sandwich folds are colored as in Figure 3, with inserted sequences shown in gray.
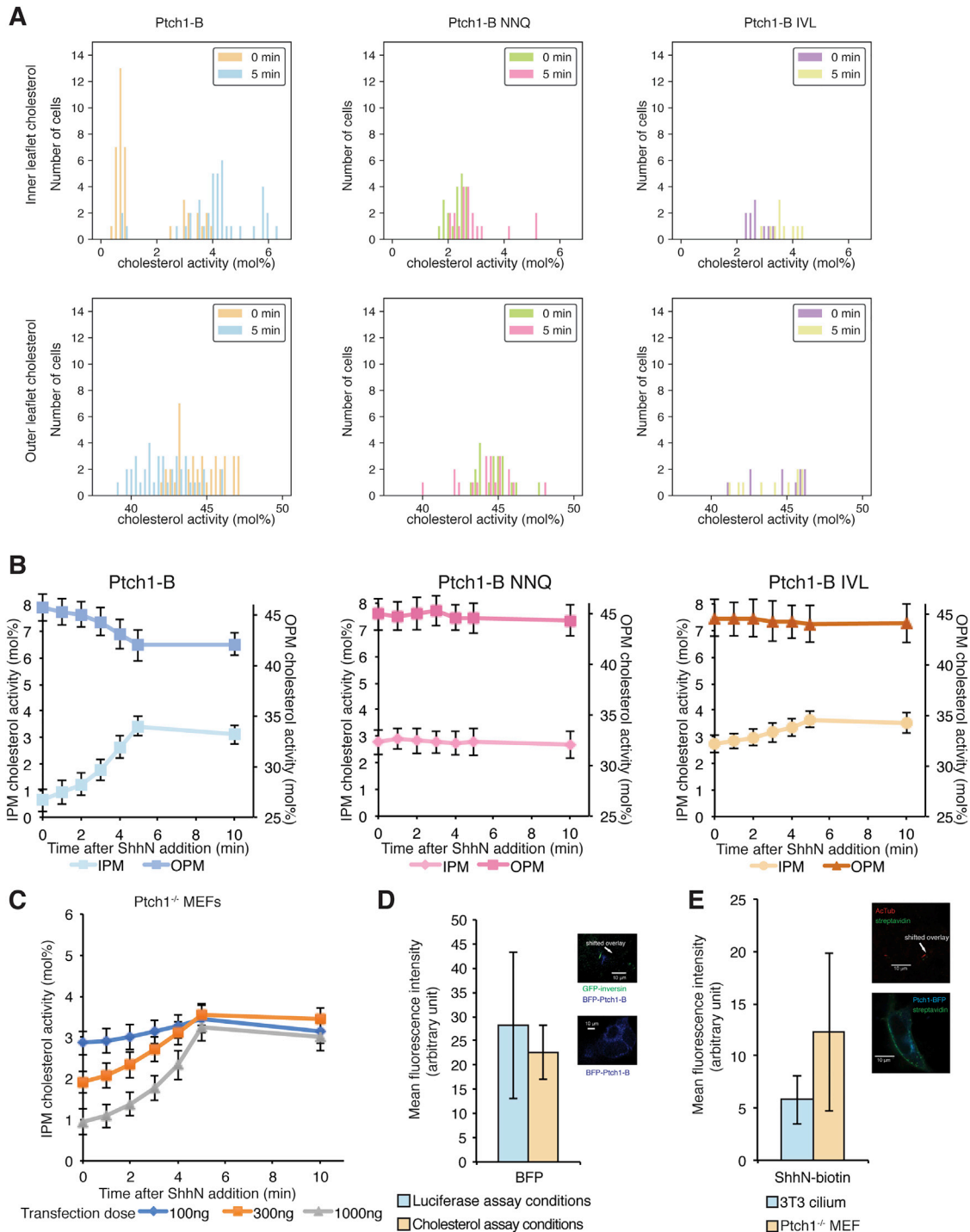
**Figure S7. PTCH1 Alters Cholesterol Distribution in the Plasma Membrane, Related to Figure 6**

(A) In Ptch1-B transfected cells, about half the cell population showed a sharp decrease in the inner leaflet cholesterol activity. Cells not showing this change likely have little or no Ptch1-B expression. Upon addition of ShhN, inner leaflet cholesterol activity was restored in most cells. In Ptch1-B NNQ transfected cells, inner leaflet cholesterol activity was within the normal range and did not change in response to ShhN. For Ptch1-B, n = 40; Ptch1-B NNQ, n = 20; Ptch1-B IVL, n = 10.

(B) Changes in IPM and OPM cholesterol activity in response to ShhN were compared between Ptch1-B, Ptch1-B NNQ, and Ptch1-B IVL. For Ptch1-B, only the subpopulation of cells showing a reduction in IPM cholesterol activity was included in this analysis. The synchronized decrease in OPM cholesterol activity and increase in IPM cholesterol activity suggest that the changes in cholesterol after ShhN addition might reflect cross-bilayer redistribution.

*(legend continued on next page)*

(C) Reduction of IPM cholesterol activity in Ptch1−/− MEFs was correlated with PTCH1 expression levels. Greater reduction in IPM cholesterol activity was seen when more Ptch1-B DNA was used for transfection. The curve for 1000 ng transfection was plotted based on the same data as in Figure 6E. At the lowest level of Ptch1-B expression, IPM cholesterol activity was reduced to a level corresponding to ∼2.9 mol%. Within 5 min of ShhN addition, IPM cholesterol activity increased under all three conditions, to a level corresponding to ∼3.5%. All conditions have n = 10.

(D) BFP fluorescence from Ptch1−/− MEFs transfected with 100 ng Ptch1-B-BFP DNA was compared with the fluorescence in the primary cilium from cells transfected at a dose that permits ShhN-induced transcriptional response in a Gli-dependent luciferase assay. GFP-tagged inversin (NPHP2) was used to mark the primary cilium. The mean fluorescence intensity of the entire cell prepared for cholesterol assays was similar to the intensity in the cilium of cells prepared for the luciferase assay. Representative images are shown in the inset. For ciliary fluorescence, n = 32. A total of 37 inversin-positive cilia were observed, but 5 were excluded from the analysis due to the absence of BFP signal, as co-transfection of BFP and GFP plasmids inevitably leaves some cells expressing one construct. For cells prepared for cholesterol assays, n = 86.

(E) 3T3 cells and 100 ng transfected Ptch1−/−MEFs were stained with ShhN-biotin, and then Alexa 647 streptavidin. Streptavidin fluorescence indicates PTCH1 levels in the membrane. The primary cilium of 3T3 cells was marked by staining for acetylated tubulin. Mean fluorescence intensity of the 3T3 cilium and the MEF cell surface was within a similar range. For 3T3, n = 110. For MEFs, n = 71. Error bars indicate SEM. Representative images of cells are shown in the inset.